PCCP

ROYAL SOCIETY OF CHEMISTRY

PAPER

Cite this: *Phys. Chem. Chem. Phys.*, 2024, **26**, 9005

Implications for new particle formation in air of the use of monoethanolamine in carbon capture and storage†

Véronique Perraud, * Kanuri Roundtree, Patricia M. Morris, James N. Smith * and Barbara J. Finlayson-Pitts

Received 23rd January 2024,
Accepted 26th February 2024

DOI: 10.1039/d4cp00316k

rsc.li/pccp

Alkanolamines are currently being deployed in carbon capture and storage (CCS) technology worldwide, and atmospheric emissions have been found to coincide with locations exhibiting elevated concentrations of methanesulfonic acid (MSA). It is thus critical to understand the fate and potential atmospheric reactions of these chemicals. This study reports the characterization of sub-10 nm nanoparticles produced through the acid–base reaction between gas phase monoethanolamine (MEA) and MSA, a product of organosulfur compound oxidation in air, using a flow reactor under dry and humid (up to ~60% RH) conditions. Number size distribution measurements show that MEA is even more efficient than methylamine in forming nanoparticles on reaction with MSA. This is attributed to the fact that the MEA structure contains both an $-NH_2$ and an $-OH$ group that facilitate hydrogen bonding within the clusters, in addition to the electrostatic interactions. Due to this already strong H-bond network, water has a relatively small influence on new particle formation (NPF) and growth in this system, in contrast to MSA reactions with alkylamines. Acid/base molar ratios of unity for 4–12 nm particles were measured using thermal desorption chemical ionization mass spectrometry. The data indicate that reaction of MEA with MSA may dominate NPF under some atmospheric conditions. Thus, the unique characteristics of alkanolamines in NPF must be taken into account for accurate predictions of impacts of CCS on visibility, health and climate.

Introduction

Monoethanolamine ($NH_2CH_2CH_2OH$, MEA) is a multifunctional amine currently deployed in carbon capture and storage (CCS) technology systems aimed at sequestering CO_2 emissions before release into the atmosphere.[1–5] The most widely used CCS media is a 30% aqueous solution of MEA.[6] Briefly, the solvent medium chemically absorbs CO_2 contained in the flue gas, which leads to a CO_2-depleted gas stream exiting the stack. The solvent is subsequently regenerated and recycled back into the absorber column, while the CO_2 is compressed and captured. A potential drawback from these technologies is the likely release of MEA into the air.[4,5,7–14] For example, concentrations of MEA outside a CCS-equipped plant of the order of several ppb have been reported.[7] MEA is also used as a solvent in various consumer products and industrial processes.[15–19] In air, recognized fates of gas phase MEA to date include its reaction with O_3 and OH,[20–24] the formation of alkylaminium nitrate salts from its interaction with HNO_3[21,24] and acid–base reactions with gas phase and particulate sulfuric acid.[25,26]

Methanesulfonic acid (CH_3SO_3H, MSA) is a strong acid formed along with SO_2 (a sulfuric acid precursor) in the oxidation of dimethyl sulfide (DMS) and dimethyl disulfide (DMDS)[27–32] which have a variety of sources both natural and anthropogenic.[33–59] Therefore, it is not surprising that the oxidation product MSA is detected in the gas phase and in ambient particles worldwide. Ambient gas phase atmospheric concentrations of MSA range from mid-10^4 to 10^7 molecules cm^{-3},[60–69] and can reach levels similar to that of H_2SO_4, which is considered to be a major source of new particles. In some instances, the MSA concentration in air can actually surpass that of co-located H_2SO_4.[68,70] MSA has also been detected in ambient particles worldwide, including in marine and coastal environments,[71–77] in coastal areas affected by biomass burning plumes,[78,79] and near agricultural regions as well as near urban centers.[78,80,81] This acid has been detected in ultrafine and nucleation mode particles measured in the Arctic,[76,82–85] at urban sites[86,87] and in the Antarctic[88] as well as in a boreal

Department of Chemistry, University of California Irvine, Irvine, CA 92697, USA. E-mail: vperraud@uci.edu, jimsmith@uci.edu; Fax: +1 (949) 824-2420; Tel: +1(949) 824-2673, +1 (949) 824-9518

† Electronic supplementary information (ESI) available: Experimental methods as well as 15 Fig. S1–S15. See DOI: https://doi.org/10.1039/d4cp00316k

forest.[67,89] Particulate MSA concentrations in the Arctic summertime have been observed to correlate well with new particle formation (NPF)[85,90–94] suggesting a role for MSA in the earliest stages of NPF and growth. Chen and co-workers[95] predicted that the total annual MSA budget would be 20 Gg S y^{-1} from DMS oxidation reactions alone. However, climate change is dramatically modifying the extent of ice sheet coverage, exposing more sea water, which increases phytoplankton productivity and DMS emissions and thus MSA in air.[94,96–98] The significant contribution of MSA to atmospheric NPF is supported by both laboratory experiments[99–107] and quantum chemical calculations.[108–115]

Amines and MSA are both found in ambient particles.[67,80,116–118] This includes MEA, which has been detected as one of the most abundant amines in ambient particles in various locations around the globe,[119–124] overlapping with sources of both DMS and MSA. MEA has also been detected in biomass burning aerosols collected in St John, Newfoundland, Canada[125] and in both aerosol and precipitation samples over the North Atlantic Ocean.[126]

It is thought that NPF is responsible for a significant portion of the global cloud condensation nuclei budget.[127] In addition to influencing cloud properties, airborne particles are well known to interact with solar radiation, thus playing a critical role in the Earth's climate.[128,129] In a recent study, Hodshire *et al.*[130] predicted, using a simplified DMS oxidation model, that inclusion of MSA formation and its role in aerosol processes (either acting as condensable non- or semi-volatile species, or participating in NPF) influenced the cloud-albedo aerosol indirect and the direct radiative effect.

While recent theoretical studies predicted that MEA may play an important role in NPF,[108] to date there have been no direct experimental investigations of particle formation from MEA and MSA. We present the first measurements of 4–12 nm nanoparticles formed from this reaction, including their size distributions as a function of time and relative humidity, as well as their size-resolved chemical composition. For comparison, some data for the reaction of MSA with methylamine (MA), which is known to efficiently form particles,[102,103,105,106] is also reported. It is shown that MEA is even more effective in forming new nanometer-sized particles than MA but surprisingly, is not very sensitive to the presence of water vapor. Such ultrafine particles are of particular concern as they can be deposited deep into the respiratory tract and even cross cellular membranes to reach other organs.[131–136] Thus, this study has important implications for the potential impacts of CCS on climate,[128,129] visibility[137–140] and health.[131,132,136,141]

Experimental methods

Flow reactor description

Particles were produced from the reaction of gas phase MSA with gas phase MEA (or MA) in the presence or absence of water vapor in a 1-m long borosilicate glass flow reactor[142] described in the ESI† (Fig. S1). Clean, dry air was provided by a purge air generator (Parker-Balston; model 75-62), and further purified by passing through carbon/alumina media (PermaPure, LLC) and a 0.01 μm inline filter (Parker Balston, BQ). Most of the air was supplied at the front end of the flow reactor through the perforated ring inlets as indicated in Fig. S1 (ESI†) (rings A, B and C). In experiments where water vapor was present, one or two bubblers filled with nanopure water (18.2 MΩ cm; Barnstead, Thermo Scientific) were used to humidify a fraction of the air introduced into the ring inlets. The bubblers were kept in a water bath to maintain a constant temperature of 22 °C (295 K). Experiments were carried out at relative humidities (RH) up to ~60% as indicated by a humidity probe (Vaisala; model HMT 838) located at the end of the flow reactor. The reactants (MSA and MEA or MA) were introduced through the spoke inlets (spoke 2 and 3 respectively) located 60 cm downstream of the last ring inlet. The flow reactor was cleaned regularly with nanopure water and dried with clean hot air overnight (T = 343 K). After cleaning, the flow reactor was conditioned with gas-phase MSA for a least two days prior to an experiment. All experiments presented in this work were performed at 1 atm and at room temperature (T = 297 K).

Reactants

Liquid monoethanolamine ($NH_2CH_2CH_2OH$, Sigma Aldrich, >99.5%) was contained in a small 2-mL glass vial with a septum cap. Approximately ~1 cm of PEEK tubing (1.59 mm O. D. × 0.18 mm I. D.) was inserted into the septum so that the MEA from the headspace diffused slowly into a stream of air. For comparison, parallel experiments were performed using MA (CH_3NH_2) with a commercial permeation tube (VICI Metronics). The amine vial (or permeation tube) was inserted into separate *U*-shaped glass tubes immersed into a water bath maintained at room temperature (T = 295 K). Glass beads were placed in the upstream arm of the *U*-shaped glass tubes to provide high surface area to keep the gas flow at a constant temperature. Air flowed through each tube at a rate of 215 cm^3 min^{-1} for MEA and 93 or 211 cm^3 min^{-1} for MA. For MSA, air (53 to 216 cm^3 min^{-1}) flowed directly over the pure liquid (Sigma Aldrich, >99.0%) contained in a glass trap which was maintained at room temperature using a water bath. Further details regarding the sampling, analysis and quantification of the gas phase reactants are given in the ESI† (Text S1 and Fig. S2). The initial concentrations of the reactants after dilution in the flow reactor were (1.7–6.8) × 10^{10} molecules cm^{-3} for MSA (0.7–2.8 ppb), (3.7–8.1) × 10^{10} molecules cm^{-3} for MEA (1.5–3.3 ppb) and (11.8–26.6) × 10^{10} molecules cm^{-3} for MA (4.8–10.8 ppb). Note that these concentrations represent upper limits as they do not account for potential wall losses.

Particle size distribution measurements

Particle size distributions were continuously measured using a moveable stainless steel sampling line (0.64 cm O. D. × 0.46 cm I. D.) located inside the flow reactor along the centerline and placed at distances ranging from 3 to 43 cm away from spoke 2 (*i.e.*, the MSA addition port). All particle size distributions reported in this study are number size distributions, unless stated otherwise. These distances correspond to reaction times

in the reactor ranging from 0.3 to 4.5 s (total flow rate 23.4 L min^{-1}) or 0.5 to 7.7 s (total flow rate 10.7 L min^{-1}) based on a conversion factor determined in previous studies.[99] Note that the amine addition port is introducing the reactant backward into the flow stream so that the reaction of MSA with MEA (MA) is occurring in between spoke 2 and 3, and we chose the MSA addition port as our $t = 0$ reaction time. It is expected that the residual reactants present in the stream exiting the flow reactor are lost to the walls of the small (I.D. 0.46 cm) sampling line. Therefore, the reaction times reported are those in the flow reactor, but these could be underestimated if the reaction continues in the sampling line (residence time ~0.3–0.4 s) and the connection to the SMPS (residence time ~0.8 s). Particle losses through the sampling lines to the SMPS were accounted for as described in the ESI† (Text S2 and Fig. S3). The shortest reaction time accessible (*i.e.* 0.3 s or 0.5 s depending on the total flow in the flow tube, that was 23.4 or 10.7 L min^{-1} respectively) is expected to be the most vulnerable to residence time artefacts. This was tested by sampling at different flow rates through the sampling line (2.4 to 4.8 L min^{-1}), for a given experiment conducted at 0.5 s. Results presented in Fig. S4 (ESI†) show no change in the size distribution measured at all flow rates and suggest that reaction in the sampling line is not significant.

Size distributions were measured using a scanning mobility particle sizer (SMPS) consisting of a ^{210}Po radioactive source (10 mCi; NRD LLC; model P-2021), an electrostatic classifier (model 3080; TSI Inc.) equipped with a nano-differential mobility analyzer (nano-DMA; model 3085; TSI, Inc.), and a butanol-based ultrafine condensation particle counter (UCPC; model 3776; TSI, Inc.). To prevent buildup of the reactants in the SMPS during sampling, the sheath air inside the DMA was not recirculated, but instead air was provided by the purge air generator (15 L min^{-1}) and a vacuum pump connected to the sheath air flow pulled the sheath air out of the DMA. The aerosol flow was set to 1.5 L min^{-1}, which provided measurements of the size distributions over a mobility diameter range of 2.5 to 64 nm. The software AIM v9 (TSI, Inc.) was used to record and process the data. Particles were observed to be stable for long periods of time (Fig. S5, ESI†), allowing for size-resolved measurements that took up to 20 min per scan to yield enough mass for mass spectrometric analysis.

Size-resolved chemical composition measurements

Nanoparticles with diameters ranging from 4 to 12 nm were sampled using a thermal desorption chemical ionization mass spectrometer (TDCIMS)[105,143–146] which was connected to the same sampling line as the SMPS. The particle stream was sampled through two inlets, each equipped with a ^{210}Po unipolar charger (UPC)[143,147] to generate negatively charged particles. At each inlet, particles were subsequently size-selected using a radial nano-DMA (rDMA) running in either high resolution mode with a sheath flow of 10 L min^{-1} and an aerosol flow of 1.0 L min^{-1} through each nano-rDMA, or low resolution mode with a sheath air flow of 5.0 L min^{-1} and an aerosol flow rate of 1.6 L min^{-1} through each nano rDMA.[148] For both conditions, instead of recirculating the sheath gas within the nano-DMA, gaseous N_2 produced from the headspace of a liquid N_2 dewar was used as the sheath flow to prevent the accumulation of gas-phase MSA or MEA, and a vacuum pump was used at the DMA sheath flow outlet. The particles were collected on the tip of a Pt filament by electrostatic precipitation (applied high voltage of +3.5 kV). The filament was continuously flushed with an additional 1.25 L min^{-1} flow of N_2 to minimize sampling artifacts from gas-phase species. To select particles with a defined mobility diameter, the voltage on each rDMA was varied from 30 to 325 V. Note that the use of two separate inlets, which merged at the collection wire region, increases the flux and mass of particles that are collected on the wire without sacrificing the rDMA resolution.

The TDCIMS was run in positive ion mode to measure MEA with $(H_2O)_nH^+$ as the reagent ions (n = 0–3), and in negative ion mode to measure MSA with $(H_2O)_nO_2^-$ as the reagent ions from the presence of trace amounts of H_2O and O_2, respectively, in the carrier N_2 gas. Monoethanolamine was detected as two major ions in the mass spectra, the parent $[M + H]^+$ ion (m/z 62) and a fragment ion corresponding to $[M + H–H_2O]^+$ (m/z 44). The fragmentation of the parent $[M + H]^+$ ion of MEA is consistent with early experimental and theoretical studies[149,150] showing that although the amino group is the favored protonation site due to its higher proton affinity compared to the alcohol group,[151] rearrangement and the loss of H_2O dominates over the loss of NH_3. The corresponding fragment ion associated with the loss of NH_3 (m/z 45) was not observed in any of the mass spectra. MSA was detected in negative ion mode as the parent deprotonated $[M - H]^-$ ion (m/z 95) followed by a major fragment ion at m/z 80 (SO_3^-), with additional minor ions at m/z 64 (SO_2^-), m/z 96 (SO_4^-), m/z 97 $(HSO_4)^-$ and m/z 112 (SO_5^-). Both positive and negative mass spectra are presented in Fig. S6 (ESI†). From the desorption profiles presented in Fig. S7 (ESI†), it is evident that MEA (and MA; data not shown) desorbs first from the filament followed by MSA, consistent with the differences in their respective saturation vapor pressures (P_{sat}) at 298 K: P_{sat}(MEA) = 3.4 × 10^{-4} atm[152] and P_{sat}(MSA) = 7.4 × 10^{-7} atm.[153] Additional details on the TDCIMS analysis are described in the ESI† (Text S3–S5 and Fig. S6–S11).

Results and discussion

Fig. 1 represents the size distributions of particles from the MSA + MEA reaction under dry conditions, with each panel (A–F) representing a different reactant concentration condition. Varying reactant concentrations were achieved by either increasing or decreasing the flow of the reactant that was introduced into the flow tube, or by changing the total flow rate in the flow tube (23.4 L min^{-1} for panels (A–C); 10.7 L min^{-1} for panels (D–F)). Clearly, mixing gas phase MSA and MEA at low ppb levels results in rapid formation of particles. Corresponding plots of the evolution of the total number concentration as well as the geometric diameter as a function of the reaction time are

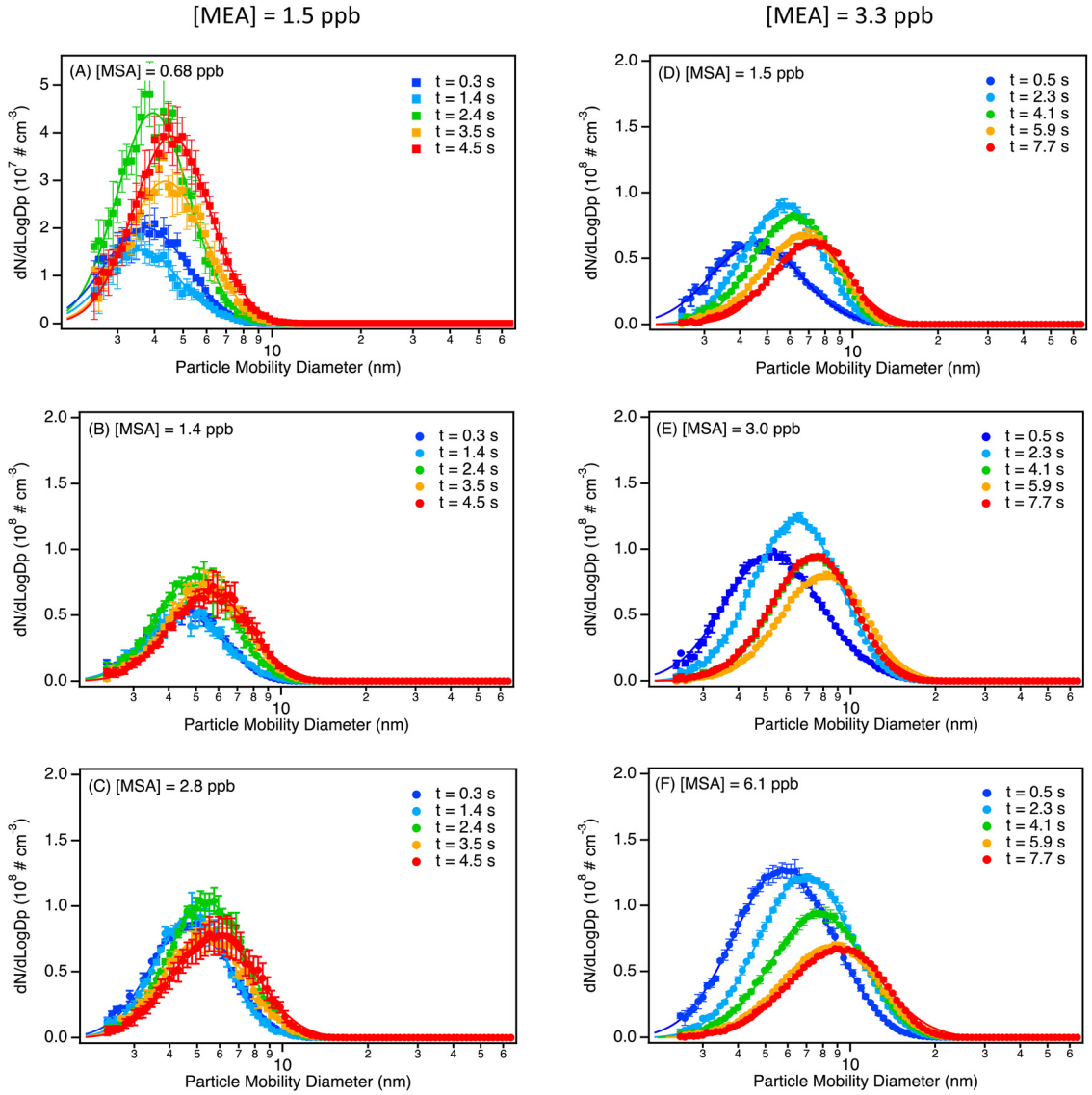

Fig. 1 Size distributions of particles from MEA (1.5 ppb) reacting with (A) 0.68 ppb MSA, (B) 1.4 ppb MSA and (C) 2.8 ppb MSA, and size distribution from MEA (3.3 ppb) reacting with (D) 1.5 ppb MSA, (E) 3.0 ppb MSA and (F) 6.1 ppb MSA. Measurements were conducted at the same sampling ports distributed equally along the length of the flow tube, but experiments displayed in panel (A)–(C) were performed with a total flow rate of 23.4 L min^{-1} (resulting in reaction times between 0.3 and 4.5 s), while experiments displayed in panel (D)–(F) were performed with a total flow rate of 10.7 L min^{-1} (resulting in reaction times between 0.5 and 7.7s). All experiments were performed under dry conditions, and size distributions are the average of 3 to 8 replicates (error bars correspond to one standard deviation) for each reaction time. All size distributions were corrected for particle losses through the sampling lines. Total particle concentrations and geometric mean diameters as a function of reaction times are given in Fig. S12 (ESI†).

presented in Fig. S12 (ESI†). Even at the smallest reactant concentrations (Fig. 1(A), 1.5 ppb MEA, 0.68 ppb MSA), particles measured at the shortest reaction time (t = 0.3 s; total flow rate 23.4 L min^{-1}) are formed at a number concentration of 6.3×10^6 particles cm^{-3} with a geometric mean mobility diameter (GMD) of $\sim$ 4 nm. At 2.4 s, the number concentration increases by a factor of two with little change in size. At longer times, there is no further increase in the particle number concentration while the particles continue to grow to a GMD of $\sim$4.6 nm, suggesting that under these conditions there is a balance between nucleation, growth by addition of the reactants onto particles, and coagulation. Particle losses inside the flow tube were estimated using the particle loss calculator tool developed by von der Weinder *et al.*[154] (using a density of 1 g cm^{-3}), and was found to be small for all diameters (*e.g.* for a particle diameter of 2.5 nm, particle transmission is predicted to be 92 or 95% for a total flow rate inside the flow tube of 10.7 or 23.4 L min^{-1}).

Similar behavior is seen as the initial MSA concentration is increased, but with larger total particle number concentrations formed (Fig. 1(B), (C) and Fig. S12A, B, ESI†). In this case, at longer reaction times the particle number concentrations start to decrease and the GMD increases due to coagulation (Fig. 1(C)). Similar, but more pronounced, trends are seen at an initial MEA concentration of 3.3 ppb and increasing MSA

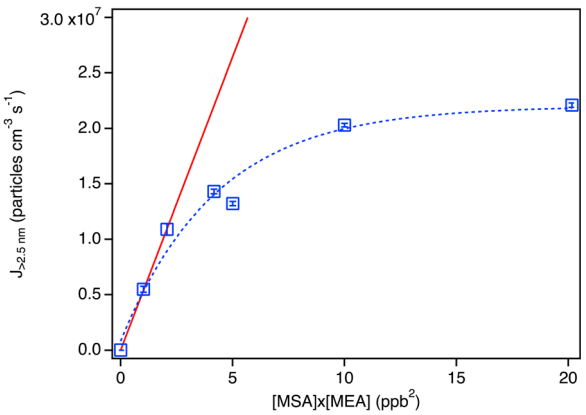

Fig. 2 Particle formation rate ($J_{>2.5\,nm}$) for the MSA + MEA system under dry conditions as a function of the product of the MSA and MEA mixing ratios in ppb. Each data point represents an average over 3 to 8 individual SMPS scans taken at 2.3–2.4 s reaction time, with error bars representing one standard deviation, and corrected for particle losses through the sampling lines. The red line is a linear fit to the data ([MSA] × [MEA] ≤ 2 ppb^2) with a slope of (5.3 ± 0.03) × 10^6 particles cm^{-3} ppb^2.

concentrations (Fig. 1(D)–(F)). For approximately the same MSA concentration (Fig. 1(B), (D) and Fig. 1(C), (E)), doubling the concentration of MEA leads to an increase in total number concentration of a factor of ∼1.2–1.4 at 2.3–2.4 s reaction time, with an increase in diameter from 4.9 to 5.6 nm (MSA = 1.4–1.5 ppb) and from 5.3 to 6.3 nm (MSA = 2.8–3.0 ppb).

For the low concentration series, the formation of approximately half of the peak particle concentration at the first measurement time implies that the rate-determining step is fast. There is some uncertainty in the exact reaction time for this first data point since it does not take into account possible continued reaction in the sampling lines. However, a half-life of ∼0.5 s for the reaction of MSA with excess MEA at 1.5 ppb (Fig. 1(A)), is consistent with a gas phase bimolecular reaction rate constant for MEA with MSA of approximately 4×10^{-11} cm^3 molecules^{-1} s^{-1}.

The particle formation rate ($J_{>2.5nm}$) was estimated using the total concentration of particles measured at ∼2.4 s (peak concentration) for all conditions, and dividing by the reaction time in seconds. Fig. 2 shows the resulting $J_{>2.5nm}$ values as a function of the product of the MEA and MSA initial concentrations. There is an initial rapid increase which is approximately linear out to [MEA] × [MSA] ∼ 2 ppb^2, suggesting that the initial 1 : 1 cluster formation is the rate-determining step. The drop-off at higher concentrations reflects coagulation. This is consistent with the TDCIMS measurements (Fig. 3), which show that the acid/base molar ratios in the particles from 4–12 nm remains within experimental error of one. All measurements were performed at 4.5 s reaction time and at an initial concentration of [MEA] of 1.5 ppb. There were no significant differences in the measured molar ratio across these experiments performed with MSA concentrations ranging from 0.68 to 2.8 ppb and the data obtained for all MSA concentrations was averaged together.

MSA concentrations in air can be as high as 10^7 molecules cm^{-3} (∼0.4 ppt)[60,61,66,68] and MEA in the low ppb range has been recorded outside a CCS facility.[7] The slope of the line in Fig. 2 at the lowest reactant concentrations is (5.3 ± 0.03) × 10^6 particles cm^{-3} ppb^{-2} so a NPF rate from the upper limit atmospheric concentrations of MEA (10 ppb) and MSA (0.4 ppt) of as much as ∼21 200 particles cm^{-3} is predicted. This can be compared to a range of formation rates of particles >3 nm diameter (J_3) from sulfuric acid of 0.001–10^5 cm^{-3} observed in different environments around the world.[155] In short, even for conditions where MEA and MSA concentrations are less than the reported maxima, this single reaction system may contribute significantly to NPF and its importance may increase as MEA use in CCS increases, and MSA increases due to a warming climate.

Efficient particle formation from MEA and MSA is consistent with the excellent stability at room temperature and low vapor pressure of the MSA–MEA salt synthesized by Greaves and co-workers.[156] Furthermore, MEA–MSA has been reported to have properties of a protic ionic liquid, even though it remains a solid at room temperature.[156–159] Its properties include a glass transition of −44 °C, melting point of about 100 °C, and a thermal stability up to 286–323 °C for the fused salt.[156]

Tropospheric air contains significant amounts of water vapor, hence the impact of relative humidity (RH) on particle formation from MEA + MSA was also examined. Surprisingly,

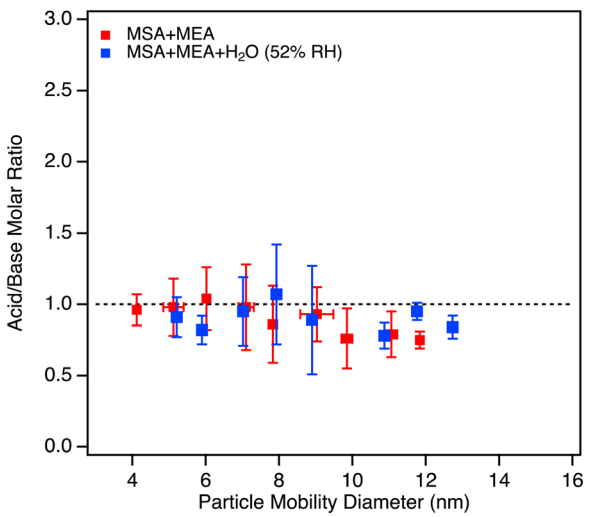

Fig. 3 Acid/base molar ratios measured by the TDCIMS for the MSA + MEA system, under dry conditions (red data points) and at 52% RH (blue data points) collected at 4.5 s reaction time. MEA was measured in POS ion mode while MSA was measured in NEG ion mode, and the ion distributions in the MS spectra were similar at all reactant concentrations (Fig. S6, ESI†). Text S5 provides more detailed information on how the acid/base molar ratios were estimated. All measurements were performed with initial MEA concentration of 1.5 ppb. No significant difference was observed in the measured molar ratio across for experiments performed with [MSA] = 0.68 ppb, [MSA] = 1.4 ppb or [MSA] = 2.8 ppb, in either dry or humid conditions; thus the data points represent average values across the [MSA] concentrations range for each RH condition. For each data point, the error bars represent one standard deviation. The dashed line corresponds to an acid/base molar ratio of unity for reference.

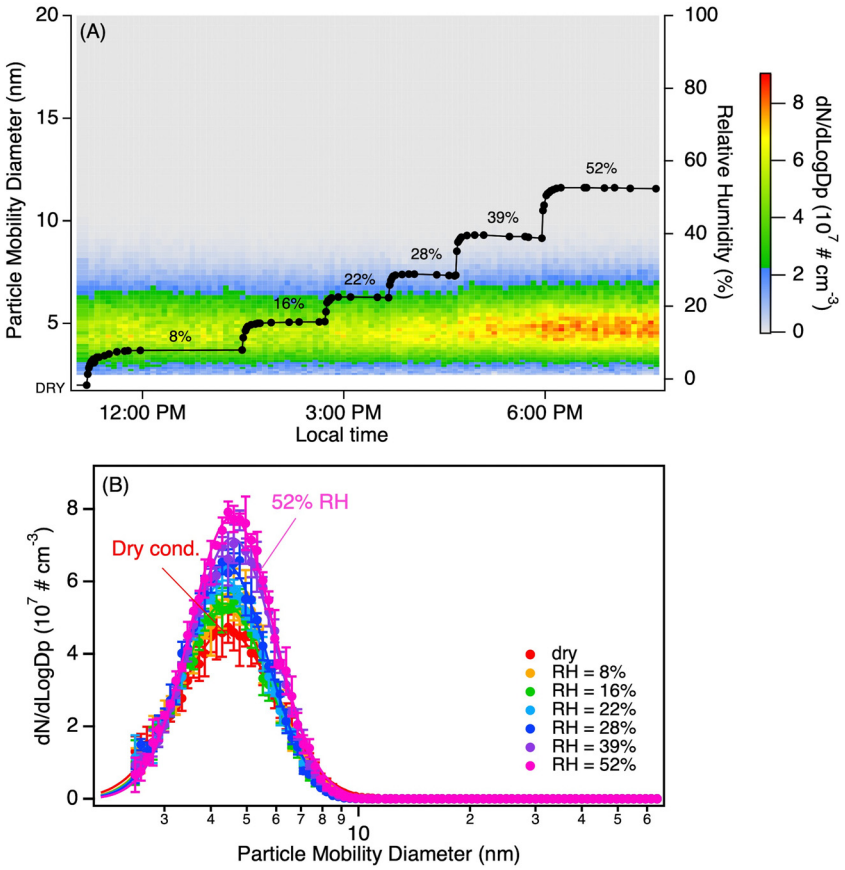

Fig. 4 Evolution of the particle size distributions as a function of relative humidity (RH) from the reaction of MSA (0.7 ppb) with MEA (1.4 ppb). Panel (A) represents the evolution as a function of time while panel (B) represents a snapshot of the size distributions at a given RH (each distribution is an average over three SMPS scans with the error bars representing one standard variation). All measurements were performed at 4.5 s reaction time, and particle size distributions were corrected for particle loss through the sampling lines.

and in contrast to previous results obtained for small alkylamines, the addition of water vapor to the MSA + MEA system did not significantly increase the number concentration at RH below ~20% as indicated in Fig. 4. Fig. 5(A) and (B) shows the evolution of the particle size distributions as a function of time at an RH of ~50% for two different sets of precursor concentrations corresponding to the dry conditions presented in Fig. 1(A) and (C) respectively. The evolution of the size distributions as a function of time in the flow reactor is similar to that observed under dry conditions. To better compare the dry *versus* humid case, total particle concentrations and geometric mean diameters measured at 4.5 s over several repeated experiments were averaged and are shown in Fig. S13 (ESI†). The addition of water vapor increased the total number concentration by only a factor of 1.3–1.5 as indicated by the bars. Note that the enhancement factor (EF) measured at 4.5 s for the high MSA, high RH case is an underestimate as it already includes coagulation (Fig. 5(C)). At the peak particle concentration (t = 1.4 s reaction time), EF = 1.9. There is only a small increase in size (red squares) at the highest MSA concentrations.

Classical nucleation theory predicts that the number of water molecules in the critical cluster can, under some conditions, be obtained from the slope of a log–log plot of the formation rate of new particles *versus* the gas phase water concentration.[160] However, this is highly dependent on a number of assumptions.[161] As seen in Fig. 6, there is no significant correlation with H_2O concentration. This could indicate that water is not a central ingredient in the critical cluster formed from MEA and MSA. Alternatively, it could be due to the absence of an energy barrier in the reaction so the slope simply reflects a lack of particle formation rate on the water concentration.[161] Furthermore, no change in the acid/base molar ratio was observed in the TDCIMS measurements in the presence of water compared to the dry case (Fig. 3; blue data points) indicating that the particles remained neutral. This lack of dependence on water is in contrast to previous results obtained for the small alkylamines,[102] where a slope of 1.3–2.3 in the log–log plot was observed.

Shen *et al.*[108] carried out computational studies of cluster formation from MEA and MSA, They showed that the 1 : 1 cluster was the least stable and hence formation of this cluster is the rate-determining step. This is consistent with the measured rates of particle formation depending on the product of the MEA and MSA concentrations and the 1 : 1 acid/base ratio of the particles. They demonstrated that the binding of MEA and MSA was determined by a combination of proton transfer from

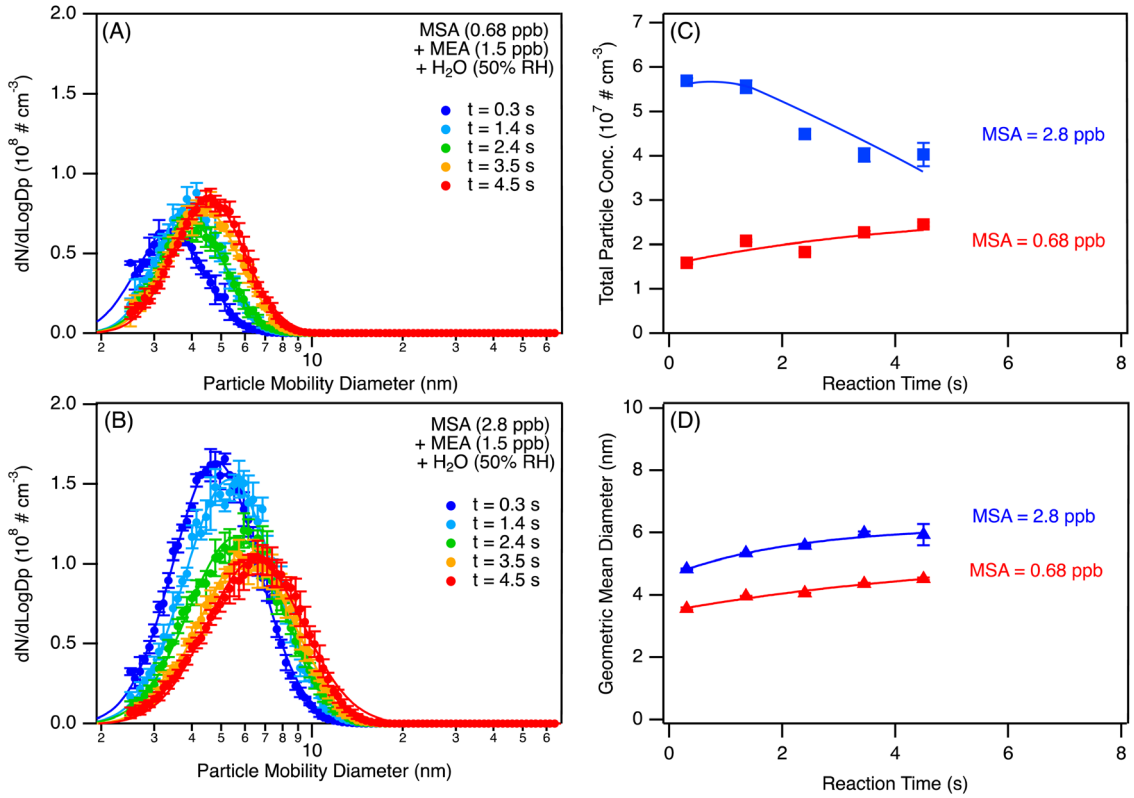

Fig. 5 Size distributions (A) and (B) and evolution of the particle total concentrations and geometric mean diameters measured as a function of the reaction time (C) and (D) in the flow reactor for the MSA + MEA reaction system at 50% RH. All lines in panels C and D are guides to the eye. All data originate from replicate scans (n = 5) and are displayed with one standard deviation. All size distributions were corrected for particle losses through the sampling lines.

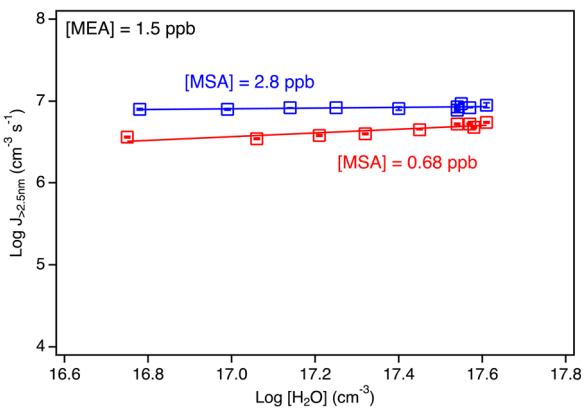

Fig. 6 Logarithm of the particle formation rate ($J_{>2.5\ nm}$) for the MSA + MEA system under humid conditions (RH ranging from 8 to 56%) as a function of the log of the water concentration (in molecules cm^{-3}). Each data point represents an average over 3 to 6 individual SMPS scans taken at 4.5 s reaction time, with error bars representing one standard deviation. All data points were corrected for particle loss through the sampling line. Red data are for [MSA] = 0.68 ppb and [MEA] = 1.5 ppb while the blue data are for [MSA] = 2.8 ppb and [MEA] = 1.5 ppb. The slopes of the lines are 0.04 for 2.8 ppb MSA and 0.2 for 0.68 ppb MSA.

the acid MSA to the nitrogen of the MEA base, along with hydrogen bonding. MEA differs from simple amines in that it has both the $-NH_2$ group as well as the –OH group, providing more than one hydrogen-bonding opportunity to MSA. Indeed, in all acid–base clusters, MSA acted as a H-bond donor and in many of the clusters, the –OH group of MEA acted as a H-bond donor to MSA. This results in strongly bound clusters held together by both electrostatic forces and a network of H-bonds, as illustrated in Fig. S14 (ESI†). It is interesting that the resulting structures have the $-CH_3$ group of MSA on the edge of the cluster, making the cluster somewhat hydrophobic. The hydrate distribution reported by Shen *et al.*[108] predicted that each cluster was predominantly hydrated by only one water molecule even at relatively high RH (80%). They also predicted that if water is present during cluster formation, it will enhance particle formation by about an order of magnitude at 50% RH due to a decrease in the evaporation rate of the initially formed 1 : 1 cluster. This predicted increase is significantly greater than the factor of 1.5–1.6 measured in these experiments.

In previous studies of NPF from MSA and amines, methylamine (MA) was shown to be the most efficient of the simple alkylamines in forming particles.[102,103,105,106] Fig. 7 compares the size distributions of particles formed from the reactions of 1.4 ppb MSA with 1.5 ppb MEA or 4.8 ppb MA under dry conditions. Even with three times the amine concentration, the total concentration of particles formed from MA is 17 times smaller than from MEA. This is consistent with previously

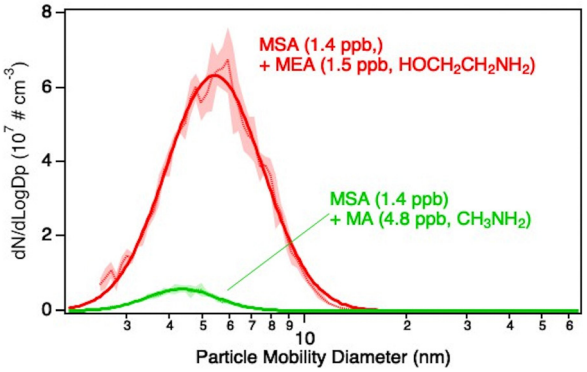

Fig. 7 Representative averaged size distribution (red trace) from the reaction of MSA (1.4 ppb) with MEA (1.5 ppb). For comparison, a size distribution for MSA (1.4 ppb) reacting with MA (4.8 ppb) is also shown (green trace). Both size distributions were taken at ~4 s reaction time. Each size distribution was averaged over five consecutive scans and the shaded area corresponds to one standard deviation uncertainty. The thick line corresponds to a log normal fit to the averaged data. Both size distributions have been corrected for particle losses through the sampling lines.

reported theoretical calculations[108,114,162] which predict a greater stability of the clusters with the increased H-bonding capability of MEA and, as a consequence, particle formation rates that are orders of magnitude higher for MSA + MEA compared to that for MSA + MA at similar concentrations. The gas phase basicity[151] of MEA (896.8 kJ mol^{-1}) compared to MA (864.5 kJ mol^{-1}) also favors particle formation from MEA, along with the increased H-bonding opportunities.

In previous experimental studies, water had a dramatic effect on NPF from MSA reacting with small alkylamines,[102,104–106,163] quite different from MEA. In the case of MA, the presence of water during particle formation led to a large increase in both number concentration and size starting at RH < 10% (Fig. S15, ESI†). Calculations indicated that the 4MSA-4MEA cluster with one water molecule, for example, resulted in a structure that had many potential hydrogen bonding sites available, allowing the cluster to grow *via* H-bonding with other species.[163] For MEA, however, the clusters already have strongly hydrogen-bonded internal networks so that opportunities for further interactions with water molecules are reduced.

To compare the relative importance of the MEA and MA reactions with MSA for particle formation under atmospheric conditions, measurements under 10–50% RH were carried out with MA (Fig. S15, ESI†). Fig. 8 shows the NPF rate ($J_{>2.5\mathrm{nm}}$) for MEA compared to that of MA as a function of the product of the reactant concentrations. The slope of the linear fit through the data for the MEA reaction is more than four times that of the MA reaction. Thus, although NPF from MA + MSA is greatly enhanced in the presence of water, the MEA reaction is still more efficient under similar conditions. This highlights the significance of alkanolamines in NPF at low concentrations and points to H-bonding as a driver for NPF with MSA.

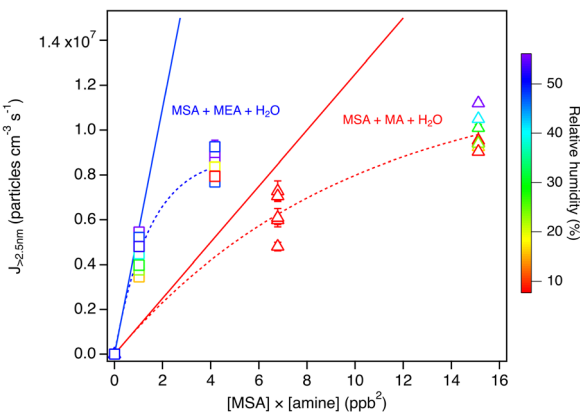

Fig. 8 Comparison between particle formation rate ($J_{>2.5\ \mathrm{nm}}$) for the MSA + MEA and the MSA + MA systems under humid conditions (RH ranging from 8 to 56%) as a function of the product of the MSA and the amine mixing ratios in ppb. Each data point represents an average over 3 to 6 individual SMPS scans taken at 4.5 s reaction time, with error bars representing one standard deviations. The dashed lines are exponential fits to the data and the solid lines are the tangent to the fits with slopes of 5.5×10^6 and 1.2×10^6 for the MSA + MEA and MSA + MA systems respectively. All data points were corrected for particle loss through the sampling lines.

Conclusions

This study shows that the acid/base interaction of MSA with a short alkanolamine widely used in CCS is quite strong and produces sub-10 nm particles extremely well compared to a simple primary alkylamine, methylamine. Water vapor has a limited impact on NPF rates as MEA has OH− groups that already promote strong H-bonding network within the clusters. This is in contrast with previous work on alkylamines where water had a large impact on nucleation and growth of new particles. The particle composition from 4–12 nm showed an acid/base molar ratio close to unity, whereas those from the MA reaction contained more acid at the smaller diameters. These findings highlight that there is not a one-size-fits-all when it comes to treating amine interactions with MSA in atmospheric models.

The overall contribution of MSA-initiated aerosol chemistry may become increasingly more important in the future.[164] For example, there is a reduction of sea-ice coverage at the poles, leading to an increase in DMS emissions[94,96–98] with an associated increase in MSA. At the same time, there has been a decline in anthropogenic SO_2 emissions over few the past decades,[165–170] with a related reduction in particulate sulfate in ambient particles in the Northern part of the globe.[167,168,171,172] Thus, MSA acid–base mediated NPF will become increasingly more important in air in the near future.

Lastly, alkanolamines are being widely deployed in CCS technology which may lead to an increase in their abundance in the atmosphere. Thus, assessing and understanding the impacts of this acid–base driven chemistry on new particle formation in air is more important than ever.

Conflicts of interest

There are no conflicts to declare.

Acknowledgements

The authors are grateful to the National Science Foundation (grants no. 1928252 and CHE-2004066) and the Army Research Office (grant no. W911NF2010064) for supporting this research. K. R. acknowledges support from the Lucille Foundation and the Chemistry Summer Undergraduate Research Fellowship (Chem-SURF). The authors thank Dr Paulus Bauer for helpful discussions during the preparation of this manuscript. The authors are also grateful to Dr Natalia Karimova and Dr R. Benny Gerber for their assistance in the DFT calculations and access to the Green-Planet Cluster at the University of California, Irvine.

References

1 G. T. Rochelle, Amine Scrubbing for CO_2 Capture, *Science*, 2009, **325**, 1652–1654.
2 C. H. Yu, C. H. Huang and C. S. Tan, A review of CO_2 capture by absorption and adsorption, *Aerosol Air Qual. Res.*, 2012, **12**, 745–769.
3 S. A. Mazari, B. S. Ali, B. M. Jan, I. M. Saeed and S. Nizamuddin, An overview of solvent management and emissions of amine-based CO_2 capture technology, *Int. J. Greenhouse Gas Control*, 2015, **34**, 129–140.
4 L. Cuccia, J. Dugay, D. Bontemps, M. Louis-Louisy and J. Vial, Analytical methods for the monitoring of post-combustion CO_2 capture process using amine solvents: A review, *Int. J. Greenhouse Gas Control*, 2018, **72**, 138–151.
5 M. Corsten, A. Ramirez, L. Shen, J. Koornneef and A. Faaij, Environmental impact assessment of CCS chains – Lessons learned and limitations from LCA literature, *Int. J. Greenhouse Gas Control*, 2013, **13**, 59–71.
6 M. Akram, K. Milkowski, J. Gibbins and M. Pourkashanian, Comparative energy and environmental performance of 40% and 30% monoethanolamine at PACT pilot plant, *Int. J. Greenhouse Gas Control*, 2020, **95**, 102946, DOI: **10.1016/j.ijggc.2019.102946**.
7 L. Zhu, G. W. Schade and C. J. Nielsen, Real-time monitoring of emissions from monoethanolamine-based industrial scale carbon capture facilities, *Environ. Sci. Technol.*, 2013, **47**, 14306–14314.
8 J. Mertens, J. Knudsen, M. L. Thielens and J. Andersen, On-line monitoring and controlling emissions in amine post combustion carbon capture: A field test, *Int. J. Greenhouse Gas Control*, 2012, **6**, 2–11.
9 J. Mertens, H. Lepaumier, D. Desagher and M. L. Thielens, Understanding ethanolamine (MEA) and ammonia emissions from amine based post combustion carbon capture: Lessons learned from field tests, *Int. J. Greenhouse Gas Control*, 2013, **13**, 72–77.
10 E. F. da Silva, H. Kolderup, E. Goetheer, K. W. Hjarbo, A. Huizinga, P. Khakharia, I. Tuinman, T. Mejdell, K. Zahlsen, K. Vernstad, A. Hyldbakk, T. Holten, H. M. Kvamsdal, P. van Os and A. Einbu, Emission studies from a CO_2 capture pilot plant, *Energy Procedia*, 2013, **37**, 778–783.
11 J. Fagerlund, R. Zevenhoven, J. Thomassen, M. Tednes, F. Abdollahi, L. Thomas, C. J. Nielsen, T. Mikoviny, A. Wisthaler, L. Zhu, C. Biliyok and A. Zhurkin, Performance of an amine-based CO_2 capture pilot plant at the Fortum Oslo Varme Waste to Energy plant in Oslo, Norway, *Int. J. Greenhouse Gas Control*, 2021, **106**, 103242.
12 M. X. Fang, N. T. Yi, W. T. Di, T. Wang and Q. H. Wang, Emission and control of flue gas pollutants in CO_2 chemical absorption system – A review, *Int. J. Greenhouse Gas Control*, 2020, **93**, 102904.
13 A. K. Morken, B. Nenseter, S. Pedersen, M. Chhaganlal, J. K. Feste, R. B. Tyborgnes, O. Ullestad, H. Ulvatn, L. Zhu, T. Mikoviny, A. Wisthaler, T. Cents, O. M. Bade, J. Knudsen, G. de Koeijer, O. Falk-Pedersen and E. S. Hamborg, Emission results of amine plant operations from MEA testing at the CO_2 Technology Centre Mongstad, *Energy Procedia*, 2014, **63**, 6023–6038.
14 K. Veltman, B. Singh and E. G. Hertwich, Human and environmental impact assessment of postcombustion CO_2 capture focusing on emissions from amine-based scrubbing solvents to air, *Environ. Sci. Technol.*, 2010, **44**, 1496–1502.
15 M. M. Fiume, B. A. Heldreth, W. F. Bergfeld, D. V. Belsito, R. A. Hill, C. D. Klaassen, D. C. Liebler, J. G. Marks, R. C. Shank, T. J. Slaga, P. W. Snyder and F. A. Andersen, Safety assessment of ethanolamine and ethanolamine salts as used in cosmetics, *Int. J. Toxicol.*, 2015, **34**, 84s–98s.
16 B. C. McDonald, J. A. de Gouw, J. B. Gilman, S. H. Jathar, A. Akherati, C. D. Cappa, J. L. Jimenez, J. Lee-Taylor, P. L. Hayes, S. A. McKeen, Y. Y. Cui, S. W. Kim, D. R. Gentner, G. Isaacman-VanWertz, A. H. Goldstein, R. A. Harley, G. J. Frost, J. M. Roberts, T. B. Ryerson and M. Trainer, Volatile chemical products emerging as largest petrochemical source of urban organic emissions, *Science*, 2018, **359**, 760–764.
17 J. Wooley, W. W. Nazaroff and A. T. Hodgson, Release of ethanol to the atmosphere during use of consumer cleaning products, *J. Air Waste Manage. Assoc.*, 1990, **40**, 1114–1120.
18 X. Ge, A. S. Wexler and S. L. Clegg, Atmospheric amines - Part I. A review, *Atmos. Environ.*, 2011, **45**, 524–546.
19 J.-A. Seo, I.-H. Bae, W.-H. Jang, J.-H. Kim, S.-Y. Bak, S.-H. Han, Y.-H. Park and K.-M. Lim, Hydrogen peroxide and monoethanolamine are the key causative ingredients for hair dye-related dermatitis and hair loss, *J. Dermatol. Sci.*, 2012, **66**, 12–19.
20 N. Borduas, J. P. D. Abbatt and J. G. Murphy, Gas phase oxidation of monoethanolamine (MEA) with OH radical and ozone: kinetics, products, and particles, *Environ. Sci. Technol.*, 2013, **47**, 6377–6383.
21 M. Karl, C. Dye, N. Schmidbauer, A. Wisthaler, T. Mikoviny, B. D'Anna, M. Muller, E. Borras, E. Clemente, A. Munoz, R. Porras, M. Rodenas, M. Vazquez and T. Brauers, Study of OH-initiated degradation of 2-aminoethanol, *Atmos. Chem. Phys.*, 2012, **12**, 1881–1901.

22 L. Onel, M. A. Blitz and P. W. Seakins, Direct determination of the rate coefficient for the reaction of OH radicals with monoethanol amine (MEA) from 296 to 510 K, *J. Phys. Chem. Lett.*, 2012, **3**, 853–856.
23 C. J. Nielsen, B. D'Anna, C. Dye, M. Graus, M. Karl, S. King, M. M. Maguto, M. Muller, N. Schmidbauer, Y. Stenstrom, A. Wisthaler and S. Pedersen, Atmospheric chemistry of 2-aminoethanol (MEA), *Energy Procedia*, 2011, **4**, 2245–2252.
24 S. M. Murphy, A. Sorooshian, J. H. Kroll, N. L. Ng, P. Chhabra, C. Tong, J. D. Surratt, E. Knipping, R. C. Flagan and J. H. Seinfeld, Secondary aerosol formation from atmospheric reactions of aliphatic amines, *Atmos. Chem. Phys.*, 2007, **7**, 2313–2337.
25 X. M. Tian, Y. X. Chu and C. K. Chan, Reactive uptake of monoethanolamine by sulfuric acid particles and hygroscopicity of monoethanolaminium salts, *Environ. Sci. Technol. Lett.*, 2022, **9**, 16–21.
26 H. B. Xie, J. Elm, R. Halonen, N. Myllys, T. Kurten, M. Kulmala and H. Vehkamaki, Atmospheric fate of monoethanolamine: enhancing new particle formation of sulfuric acid as an important removal process, *Environ. Sci. Technol.*, 2017, **51**, 8422–8431.
27 B. Rosati, S. Christiansen, R. W. de Jonge, P. Roldin, M. M. Jensen, K. Wang, S. P. Moosakutty, D. Thomsen, C. Salomonsen, N. Hyttinen, J. Elm, A. Feilberg, M. Glasius and M. Bilde, New particle formation and growth from dimethyl sulfide oxidation by hydroxyl radicals, *ACS Earth Space Chem.*, 2021, **5**, 801–811.
28 P. Van Rooy, R. Drover, T. Cress, C. Michael, K. L. Purvis-Roberts, P. J. Silva, M. J. Nee and D. Cocker, Methanesulfonic acid and sulfuric acid aerosol formed through oxidation of reduced sulfur compounds in a humid environment, *Atmos. Environ.*, 2021, **261**, 118504.
29 E. H. Hoffmann, A. Tilgner, R. Schrodner, P. Brauera, R. Wolke and H. Herrmann, An advanced modeling study on the impacts and atmospheric implications of multiphase dimethyl sulfide chemistry, *Proc. Natl. Acad. Sci. U. S. A.*, 2016, **113**, 11776–11781.
30 I. Barnes, J. Hjorth and N. Mihalopoulos, Dimethyl sulfide and dimethyl sulfoxide and their oxidation in the atmosphere, *Chem. Rev.*, 2006, **106**, 940–975.
31 R. Wollesen de Jonge, J. Elm, B. Rosati, S. Christiansen, N. Hyttinen, D. Ludemann, M. Bilde and P. Roldin, Secondary aerosol formation from dimethyl sulfide - improved mechanistic understanding based on smog chamber experiments and modelling, *Atmos. Chem. Phys.*, 2021, **21**, 9955–9976.
32 P. R. Veres, J. A. Neuman, T. H. Bertram, E. Assaf, G. M. Wolfe, C. J. Williamson, B. Weinzierl, S. Tilmes, C. R. Thompson, A. B. Thames, J. C. Schroder, A. Saiz-Lopez, A. W. Rollins, J. M. Roberts, D. Price, J. Peischl, B. A. Nault, K. H. Moller, D. O. Miller, S. Meinardi, Q. Y. Li, J. F. Lamarque, A. Kupc, H. G. Kjaergaard, D. Kinnison, J. L. Jimenez, C. M. Jernigan, R. S. Hornbrook, A. Hills, M. Dollner, D. A. Day, C. A. Cuevas, P. Campuzano-Jost, J. Burkholder, T. P. Bui, W. H. Brune, S. S. Brown, C. A. Brock, I. Bourgeois, D. R. Blake, E. C. Apel and T. B. Ryerson, Global airborne sampling reveals a previously unobserved dimethyl sulfide oxidation mechanism in the marine atmosphere, *Proc. Natl. Acad. Sci. U. S. A.*, 2020, **117**, 4505–4510.
33 S. F. Watts, The mass budgets of carbonyl sulfide, dimethyl sulfide, carbon disulfide and hydrogen sulfide, *Atmos. Environ.*, 2000, **34**, 761–779.
34 R. J. Charlson, J. E. Lovelock, M. O. Andreae and S. G. Warren, Oceanic phytoplankton, atmospheric sulfur, cloud albedo and climate, *Nature*, 1987, **326**, 655–661.
35 T. S. Bates, B. K. Lamb, A. Guenther, J. Dignon and R. E. Stoiber, Sulfur emissions to the atmosphere from natural sources, *J. Atmos. Chem.*, 1992, **14**, 315–337.
36 A. Lana, T. G. Bell, R. Simo, S. M. Vallina, J. Ballabrera-Poy, A. J. Kettle, J. Dachs, L. Bopp, E. S. Saltzman, J. Stefels, J. E. Johnson and P. S. Liss, An updated climatology of surface dimethlysulfide concentrations and emission fluxes in the global ocean, *Global Biogeochem. Cycles*, 2011, **25**, GB1004.
37 M. O. Andreae and P. J. Crutzen, Atmospheric aerosols: Biogeochemical sources and role in atmospheric chemistry, *Science*, 1997, **276**, 1052–1058.
38 V. P. Aneja, Natural sulfur emissions into the atmosphere, *J. Air Waste Manage. Assoc.*, 1990, **40**, 469–476.
39 K. Jardine, A. M. Yanez-Serrano, J. Williams, N. Kunert, A. Jardine, T. Taylor, L. Abrell, P. Artaxo, A. Guenther, C. N. Hewitt, E. House, A. P. Florentino, A. Manzi, N. Higuchi, J. Kesselmeier, T. Behrendt, P. R. Veres, B. Derstroff, J. D. Fuentes, S. T. Martin and M. O. Andreae, Dimethyl sulfide in the Amazon rain forest, *Global Biogeochem. Cycles*, 2015, **29**, 19–32.
40 P. J. Crutzen, J. Williams, U. Poschl, P. Hoor, H. Fischer, C. Warneke, R. Holzinger, A. Hansel, W. Lindinger, B. Scheeren and J. Lelieveld, High spatial and temporal resolution measurements of primary organics and their oxidation products over the tropical forests of Surinam, *Atmos. Environ.*, 2000, **34**, 1161–1165.
41 J. Kesselmeier, F. X. Meixner, U. Hofmann, A. L. Ajavon, S. Leimbach and M. O. Andreae, Reduced sulfur compound exchange between the atmosphere and tropical tree species in Southern Cameroon, *Biogeochemistry*, 1993, **23**, 23–45.
42 S. Meinardi, I. J. Simpson, N. J. Blake, D. R. Blake and F. S. Rowland, Dimethyl disulfide (DMDS) and dimethyl sulfide (DMS) emissions from biomass burning in Australia, *Geosphys. Res. Lett.*, 2003, **30**, 1454.
43 C. E. Stockwell, P. R. Veres, J. Williams and R. J. Yokelson, Characterization of biomass burning emissions from cooking fires, peat, crop residue, and other fuels with high-resolution proton-transfer-reaction time-of-flight mass spectrometry, *Atmos. Chem. Phys.*, 2015, **15**, 845–865.
44 V. Perraud, S. Meinardi, D. R. Blake and B. J. Finlayson-Pitts, Challenges associated with the sampling and analysis of organosulfur compounds in air using real-time PTR-

ToF-MS and offline GC-FID, *Atmos. Meas. Tech.*, 2016, **9**, 1325–1340.
45 S. Trabue, K. Scoggin, F. Mitloehner, H. Li, R. Burns and H. Xin, Field sampling method for quantifying volatile sulfur compounds from animal feeding operations, *Atmos. Environ.*, 2008, **42**, 3332–3341.
46 P. Hobbs and T. Mottram, New Directions: Significant contributions of dimethyl sulphide from livestock to the atmosphere, *Atmos. Environ.*, 2000, **34**, 3649–3650.
47 J. S. Vandergheynst, D. J. Cogan, P. J. Defelice, J. M. Gossett and L. P. Walker, Effect of process management on the emission of organosulfur compounds and gaseous antecedents from composting processes, *Environ. Sci. Technol.*, 1998, **32**, 3713–3718.
48 Z. G. Yi, X. M. Wang, G. Y. Sheng and H. M. Fu, Exchange of carbonyl sulfide (OCS) and dimethyl sulfide (DMS) between rice paddy fields and the atmosphere in subtropical China, *Agric., Ecosyst. Environ.*, 2008, **123**, 116–124.
49 P. D. Goldan, W. C. Kuster, D. L. Albritton and F. C. Fehsenfeld, The measurement of natural sulfur emissions from soils and vegetation – 3 Sites in the Eastern-United-States revisited, *J. Atmos. Chem.*, 1987, **5**, 439–467.
50 J. Williams, N. Y. Wang, R. J. Cicerone, K. Yagi, M. Kurihara and F. Terada, Atmospheric methyl halides and dimethyl sulfide from cattle, *Global Biogeochem. Cycles*, 1999, **13**, 485–491.
51 K. C. Li and D. Shooter, Analysis of sulfur-containing compounds in ambient air using solid-phase microextraction and gas chromatography with pulsed flame photometric detection, *Int. J. Environ. Anal. Chem.*, 2004, **84**, 749–760.
52 M. R. Ras, F. Borrull and R. M. Marce, Determination of volatile organic sulfur compounds in the air at sewage management areas by thermal desorption and gas chromatography-mass spectrometry, *Talanta*, 2008, **74**, 562–569.
53 E. Smet and H. Van Langenhove, Abatement of volatile organic sulfur compounds in odorous emissions from the bio-industry, *Biodegradation*, 1998, **9**, 273–284.
54 R. Raiswell and S. H. Bottrel, The disposal of flue gas desulphurisation waste: sulphur gas emissions and their control, *Environ. Geochem. Health*, 1991, **13**, 119–126.
55 P. R. Mulay, P. Cavicchia, S. M. Watkins, A. Tovar-Aguilar, M. Wiese and G. M. Calvert, Acute illness associated with exposure to a new soil fumigant containing dimethyl disulfide – Hillsborough County, Florida, 2014, *J. Agromedicine*, 2016, **21**, 373–379.
56 D. D. Yan, A. C. Cao, Q. X. Wang, Y. Li, C. B. Ouyang, M. X. Guo and X. Q. Guo, Dimethyl disulfide (DMDS) as an effective soil fumigant against nematodes in China, *PLoS One*, 2019, **14**, 1–9.
57 J. Fritsch, T. Fouillet, P. Charles, P. Fargier-Puech, C. Ramponi-Bur, S. Descamps, G. Du Fretay and A. Myrta, French experiences with dimethyl disulfide (DMDS) as a nematicide in vegetable crops, *Acta Hortic.*, 2014, **1044**, 427–433.
58 F. L. Suarez, J. K. Furne, J. Springfield and M. D. Levitt, Morning breath odor: Influence of treatments on sulfur gases, *J. Dent. Res.*, 2000, **79**, 1773–1777.
59 S. Meinardi, K. B. Jin, B. Barletta, D. R. Blake and N. D. Vaziri, Exhaled breath and fecal volatile organic biomarkers of chronic kidney disease, *Biochim. Biophys. Acta, Gen. Subj.*, 2013, **1830**, 2531–2537.
60 H. Berresheim, M. Adam, C. Monahan, C. O'Dowd, J. M. C. Plane, B. Bohn and F. Rohrer, Missing SO_2 oxidant in the coastal atmosphere? - Observations from high-resolution measurements of OH and atmospheric sulfur compounds, *Atmos. Chem. Phys.*, 2014, **14**, 12209–12223.
61 H. Berresheim, T. Elste, H. G. Tremmel, A. G. Allen, H. C. Hansson, K. Rosman, M. Dal Maso, J. M. Makela, M. Kulmala and C. D. O'Dowd, Gas-aerosol relationships of H_2SO_4, MSA, and OH: Observations in the coastal marine boundary layer at Mace Head, Ireland, *J. Geophys. Res.*, 2002, **107**, D19, 8100 (PAR 8105-8101 - PAR 8105-8112).
62 F. L. Eisele and D. J. Tanner, Measurement of the gas-phase concentration of H_2SO_4 and methane sulfonic acid and estimates of H_2SO_4 production and loss in the atmosphere, *J. Geophys. Res.*, 1993, **98**, 9001–9010.
63 A. Jefferson, D. J. Tanner, F. L. Eisele, D. D. Davis, G. Chen, J. Crawford, J. W. Huey, A. L. Torres and H. Berresheim, OH photochemistry and methane sulfonic acid formation in the coastal Antarctic boundary layer, *J. Geophys. Res.*, 1998, **103**, 1647–1656.
64 C. D. O'Dowd, K. Hameri, J. M. Makela, L. Pirjola, M. Kulmala, S. G. Jennings, H. Berresheim, H. C. Hansson, G. de Leeuw, G. J. Kunz, A. G. Allen, C. N. Hewitt, A. Jackson, Y. Viisanen and T. Hoffmann, A dedicated study of New Particle Formation and Fate in the Coastal Environment (PARFORCE): Overview of objectives and achievements, *J. Geophys. Res.*, 2002, **107**, 8108.
65 H. Bardouki, H. Berresheim, M. Vrekoussis, J. Sciare, G. Kouvarakis, K. Oikonomou, J. Schneider and N. Mihalopoulos, Gaseous (DMS, MSA, SO_2, H_2SO_4 and DMSO) and particulate (sulfate and methanesulfonate) sulfur species over the northeastern coast of Crete, *Atmos. Chem. Phys.*, 2003, **3**, 1871–1886.
66 L. J. Beck, N. Sarnela, H. Junninen, C. J. M. Hoppe, O. Garmash, F. Bianchi, M. Riva, C. Rose, O. Perakyla, D. Wimmer, O. Kausiala, T. Jokinen, L. Ahonen, J. Mikkila, J. Hakala, X. C. He, J. Kontkanen, K. K. E. Wolf, D. Cappelletti, M. Mazzola, R. Traversi, C. Petroselli, A. P. Viola, V. Vitale, R. Lange, A. Massling, J. K. Nojgaard, R. Krejci, L. Karlsson, P. Zieger, S. Jang, K. Lee, V. Vakkari, J. Lampilahti, R. C. Thakur, K. Leino, J. Kangasluoma, E. M. Duplissy, E. Siivola, M. Marbouti, Y. J. Tham, A. Saiz-Lopez, T. Petaja, M. Ehn, D. R. Worsnop, H. Skov, M. Kulmala, V. M. Kerminen and M. Sipila, Differing mechanisms of new particle formation at two Arctic sites, *Geosphys. Res. Lett.*, 2021, **48**, e2020GL091334.

67 M. J. Lawler, M. P. Rissanen, M. Ehn, R. L. Mauldin, N. Sarnela, M. Sipilä and J. N. Smith, Evidence for diverse biogeochemical drivers of boreal forest new particle formation, *Geosphys. Res. Lett.*, 2018, **45**, 2038–2046.

68 R. L. Mauldin, C. A. Cantrell, M. Zondlo, E. Kosciuch, F. L. Eisele, G. Chen, D. Davis, R. Weber, J. Crawford, D. Blake, A. Bandy and D. Thornton, Highlights of OH, H_2SO_4, and methane sulfonic acid measurements made aboard the NASA P-3B during Transport and Chemical Evolution over the Pacific, *J. Geophys. Res.*, 2003, **108**, 8796.

69 L. L. J. Quelever, L. Dada, E. Asmi, J. Lampilahti, T. Chan, J. E. Ferrara, G. E. Copes, G. Perez-Fogwill, L. Barreira, M. Aurela, D. R. Worsnop, T. Jokinen and M. Sipila, Investigation of new particle formation mechanisms and aerosol processes at Marambio Station, Antarctic Peninsula, *Atmos. Chem. Phys.*, 2022, **22**, 8417–8437.

70 D. Davis, G. Chen, P. Kasibhatla, A. Jefferson, D. Tanner, F. Eisele, D. Lenschow, W. Neff and H. Berresheim, DMS oxidation in the Antarctic marine boundary layer: Comparison of model simulations and field observations of DMS, DMSO, $DMSO_2$, H_2SO_4(g), MSA(g), and MSA(p), *J. Geophys. Res.*, 1998, **103**, 1657–1678.

71 E. S. Saltzman, D. L. Savoie, R. G. Zika and J. M. Prospero, Methane sulfonic acid in the marine atmosphere, *J. Geophys. Res.: Oceans*, 1983, **88**, 897–902.

72 S. Huang, L. Poulain, D. van Pinxteren, M. van Pinxteren, Z. J. Wu, H. Herrmann and A. Wiedensohler, Latitudinal and seasonal distribution of particulate MSA over the Atlantic using a validated quantification method with HR-ToF-AMS, *Environ. Sci. Technol.*, 2017, **51**, 418–426.

73 L. Phinney, W. R. Leaitch, U. Lohmann, H. Boudries, D. R. Worsnop, J. T. Jayne, D. Toom-Sauntry, M. Wadleigh, S. Sharma and N. Shantz, Characterization of the aerosol over the sub-arctic north east Pacific Ocean, *Deep Sea Res., Part II*, 2006, **53**, 2410–2433.

74 A. Sorooshian, L. T. Padro, A. Nenes, G. Feingold, A. McComiskey, S. P. Hersey, H. Gates, H. H. Jonsson, S. D. Miller, G. L. Stephens, R. C. Flagan and J. H. Seinfeld, On the link between ocean biota emissions, aerosol, and maritime clouds: Airborne, ground, and satellite measurements off the coast of California, *Global Biogeochem. Cycles*, 2009, **23**, 1–15.

75 D. D. Huang, Y. J. Li, B. P. Lee and C. K. Chan, Analysis of organic sulfur compounds in atmospheric aerosols at the HKUST supersite in Hong Kong using HR-ToF-AMS, *Environ. Sci. Technol.*, 2015, **49**, 3672–3679.

76 M. D. Willis, J. Burkart, J. L. Thomas, F. Kollner, J. Schneider, H. Bozem, P. M. Hoor, A. A. Aliabadi, H. Schulz, A. B. Herber, W. R. Leaitch and J. P. D. Abbatt, Growth of nucleation mode particles in the summertime Arctic: a case study, *Atmos. Chem. Phys.*, 2016, **16**, 7663–7679.

77 L. C. Maudlin, Z. Wang, H. H. Jonsson and A. Sorooshian, Impact of wildfires on size-resolved aerosol composition at a coastal California site, *Atmos. Environ.*, 2015, **119**, 59–68.

78 A. Sorooshian, E. Crosbie, L. C. Maudlin, J. S. Youn, Z. Wang, T. Shingler, A. M. Ortega, S. Hersey and R. K. Woods, Surface and airborne measurements of organosulfur and methanesulfonate over the western United States and coastal areas, *J. Geophys. Res.*, 2015, **120**, 8535–8548.

79 C. Stahl, M. T. Cruz, P. A. Banaga, G. Betito, R. A. Braun, M. A. Aghdam, M. O. Cambaliza, G. R. Lorenzo, A. B. MacDonald, M. R. A. Hilario, P. C. Pabroa, J. R. Yee, J. B. Simpas and A. Sorooshian, Sources and characteristics of size-resolved particulate organic acids and methanesulfonate in a coastal megacity: Manila, Philippines, *Atmos. Chem. Phys.*, 2020, **20**, 15907–15935.

80 C. J. Gaston, K. A. Pratt, X. Y. Qin and K. A. Prather, Real-time detection and mixing state of methanesulfonate in single particles at an inland urban location during a phytoplankton bloom, *Environ. Sci. Technol.*, 2010, **44**, 1566–1572.

81 H. Yuan, Y. Wang and G. S. Zhuang, MSA in Beijing aerosol, *Chin. Sci. Bull.*, 2004, **49**, 1020–1025.

82 V. M. Kerminen, M. Aurela, R. E. Hillamo and A. Virkkula, Formation of particulate MSA: Deductions from size distribution measurements in the Finnish Arctic, *Tellus B*, 1997, **49**, 159–171.

83 M. J. Lawler, E. S. Saltzman, L. Karlsson, P. Zieger, M. Salter, A. Baccarini, J. Schmale and C. Leck, New insights into the composition and origins of ultrafine aerosol in the summertime high Arctic, *Geosphys. Res. Lett.*, 2021, **48**, e2021GL094395.

84 J. Burkart, M. D. Willis, H. Bozem, J. L. Thomas, K. Law, P. Hoor, A. A. Aliabadi, F. Kollner, J. Schneider, A. B. Herber, J. D. Abbatt and W. R. Leaitch, Summertime observations of elevated levels of ultrafine particles in the high Arctic marine boundary layer, *Atmos. Chem. Phys.*, 2017, **17**, 5515–5535.

85 K. T. Park, S. Jang, K. Lee, Y. J. Yoon, M. S. Kim, K. Park, H. J. Cho, J. H. Kang, R. Udisti, B. Y. Lee and K. H. Shin, Observational evidence for the formation of DMS-derived aerosols during Arctic phytoplankton blooms, *Atmos. Chem. Phys.*, 2017, **17**, 9665–9675.

86 X. X. Li, Y. Y. Li, M. J. Lawler, J. M. Hao, J. N. Smith and J. K. Jiang, Composition of ultrafine particles in urban Beijing: Measurement using a thermal desorption chemical ionization mass spectrometer, *Environ. Sci. Technol.*, 2021, **55**, 2859–2868.

87 T. A. Pakkanen, V. M. Kerminen, C. H. Korhonen, R. E. Hillamo, P. Aarnio, T. Koskentalo and W. Maenhaut, Urban and rural ultrafine (PM(0.1)) particles in the Helsinki area, *Atmos. Environ.*, 2001, **35**, 4593–4607.

88 K. N. Fossum, J. Ovadnevaite, D. Ceburnis, M. Dall'Osto, S. Marullo, M. Bellacicco, R. Simo, D. T. Liu, M. Flynn, A. Zuend and C. O'Dowd, Summertime primary and secondary contributions to Southern ocean cloud condensation nuclei, *Sci. Rep.*, 2018, **8**, 13844.

89 J. M. Makela, S. Yli-Koivisto, V. Hiltunen, W. Seidl, E. Swietlicki, K. Teinila, M. Sillanpaa, I. K. Koponen, J. Paatero, K. Rosman and K. Hameri, Chemical composition of aerosol during particle formation events in boreal forest, *Tellus B*, 2001, **53**, 380–393.

90 M. Dall'Osto, D. C. S. Beddows, P. Tunved, R. Krejci, J. Strom, H. C. Hansson, Y. J. Yoon, K. T. Park, S. Becagli, R. Udisti, T. Onasch, C. D. O'Dowd, R. Simo and R. M. Harrison, Arctic sea ice melt leads to atmospheric new particle formation, *Sci. Rep.*, 2017, **7**, 1–10.

91 P. K. Quinn, T. L. Miller, T. S. Bates, J. A. Ogren, E. Andrews and G. E. Shaw, A 3-year record of simultaneously measured aerosol chemical and optical properties at Barrow, Alaska, *J. Geophys. Res.*, 2002, **107**, 4130.

92 W. R. Leaitch, S. Sharma, L. Huang, D. Toom-Sauntry, A. Chivulescu, A.-M. Macdonald, K. von Salzen, J. R. Pierce, A. K. Bertram, J. C. Schroder, N. C. Shantz, R. Y.-W. Chang and A.-L. Norman, Dimethyl sulfide control of the clean summertime Arctic aerosol and cloud, *Elem. Sci. Anth.*, 2013, **1**, 1–12.

93 M. Dall'Osto, R. Simo, R. M. Harrison, D. C. S. Beddows, A. Saiz-Lopez, R. Lange, H. Skov, J. K. Nojgaard, I. E. Nielsen and A. Massling, Abiotic and biotic sources influencing spring new particle formation in North East Greenland, *Atmos. Environ.*, 2018, **190**, 126–134.

94 M. D. Willis, W. R. Leaitch and J. P. D. Abbatt, Processes controlling the composition and abundance of Arctic aerosol, *Rev. Geophys.*, 2018, **56**, 621–671.

95 Q. Chen, T. Sherwen, M. Evans and B. Alexander, DMS oxidation and sulfur aerosol formation in the marine troposphere: a focus on reactive halogen and multiphase chemistry, *Atmos. Chem. Phys.*, 2018, **18**, 13617–13637.

96 M. Gali, E. Devred, M. Babin and M. Levasseur, Decadal increase in Arctic dimethylsulfide emission, *Proc. Natl. Acad. Sci. U. S. A.*, 2019, **116**, 19311–19317.

97 S. Sharma, E. Chan, M. Ishizawa, D. Toom-Sauntry, S. L. Gong, S. M. Li, D. W. Tarasick, W. R. Leaitch, A. Norman, P. K. Quinn, T. S. Bates, M. Levasseur, L. A. Barrie and W. Maenhaut, Influence of transport and ocean ice extent on biogenic aerosol sulfur in the Arctic atmosphere, *J. Geophys. Res.*, 2012, **117**, D12209.

98 S. Becagli, L. Lazzara, C. Marchese, U. Dayan, S. E. Ascanius, M. Cacciani, L. Caiazzo, C. Di Biagio, T. Di Iorio, A. di Sarra, P. Eriksen, F. Fani, F. Giardi, D. Meloni, G. Muscari, G. Pace, M. Severi, R. Traversi and R. Udisti, Relationships linking primary production, sea ice melting, and biogenic aerosol in the Arctic, *Atmos. Environ.*, 2016, **136**, 1–15.

99 K. D. Arquero, R. B. Gerber and B. J. Finlayson-Pitts, The role of oxalic acid in new particle formation from methanesulfonic acid, methylamine, and water, *Environ. Sci. Technol.*, 2017, **51**, 2124–2130.

100 K. D. Arquero, J. Xu, R. B. Gerber and B. J. Finlayson-Pitts, Particle formation and growth from oxalic acid, methanesulfonic acid, trimethylamine and water: a combined experimental and theoretical study, *Phys. Chem. Chem. Phys.*, 2017, **19**, 28286–28301.

101 H. Chen, M. J. Ezell, K. D. Arquero, M. E. Varner, M. L. Dawson, R. B. Gerber and B. J. Finlayson-Pitts, New particle formation and growth from methanesulfonic acid, trimethylamine and water, *Phys. Chem. Chem. Phys.*, 2015, **17**, 13699–13709.

102 H. Chen, M. E. Varner, R. B. Gerber and B. J. Finlayson-Pitts, Reactions of methanesulfonic acid with amines and ammonia as a source of new particles in air, *J. Phys. Chem. B*, 2016, **120**, 1526–1536.

103 H. H. Chen and B. J. Finlayson-Pitts, New particle formation from methanesulfonic acid and amines/ammonia as a function of temperature, *Environ. Sci. Technol.*, 2017, **51**, 243–252.

104 M. L. Dawson, M. E. Varner, V. Perraud, M. J. Ezell, R. B. Gerber and B. J. Finlayson-Pitts, Simplified mechanism for new particle formation from methanesulfonic acid, amines, and water via experiments and ab initio calculations, *Proc. Natl. Acad. Sci. U. S. A.*, 2012, **109**, 18719–18724.

105 V. Perraud, X. X. Li, J. K. Jiang, B. J. Finlayson-Pitts and J. N. Smith, Size-resolved chemical composition of sub-20 nm particles from methanesulfonic acid reactions with methylamine and ammonia, *ACS Earth Space Chem.*, 2020, **4**, 1182–1194.

106 V. Perraud, J. Xu, R. B. Gerber and B. J. Finlayson-Pitts, Integrated experimental and theoretical approach to probe the synergistic effect of ammonia in methanesulfonic acid reactions with small alkylamines, *Environ. Sci.: Processes Impacts*, 2020, **22**, 305–328.

107 J. S. Johnson and C. N. Jen, Role of methanesulfonic acid in sulfuric acid-amine and ammonia new particle formation, *ACS Earth Space Chem.*, 2023, **7**, 653–660.

108 J. Shen, H.-B. Xie, J. Elm, F. Ma, J. Chen and H. Vehkamaki, Methanesulfonic acid-driven new particle formation enhanced by monoethanolamine: A computational study, *Environ. Sci. Technol.*, 2019, **53**, 14387–14397.

109 J. W. Shen, J. Elm, H. B. Xie, J. W. Chen, J. F. Niu and H. Vehkamaki, Structural effects of amines in enhancing methanesulfonic acid-driven new particle formation, *Environ. Sci. Technol.*, 2020, **54**, 13498–13508.

110 H. L. Zhao, X. T. Jiang and L. Du, Contribution of methane sulfonic acid to new particle formation in the atmosphere, *Chemosphere*, 2017, **174**, 689–699.

111 F. R. Rasmussen, J. Kubecka and J. Elm, Contribution of methansulfonic acid to the formation of molecular clusters in the marine atmosphere, *J. Phys. Chem. A*, 2022, **126**, 7127–7136.

112 J. Elm, Clusteromics II: Methansulfonic acid-base cluster formation, *ACS Omega*, 2021, **6**, 17035–17044.

113 R. Zhang, J. Shen, H.-B. Xie, J. Chen and J. Elm, The role of organic acids in new particle formation from methanesulfonic acid and methylamine, *Atmos. Chem. Phys.*, 2022, **22**, 2639–2650.

114 S. Chee, K. Barsanti, J. N. Smith and N. Myllys, A predictive model for salt nanoparticle formation using heterodimer stability calculations, *Atmos. Chem. Phys.*, 2021, **21**, 11637–11654.

115 D. P. Chen, D. F. Li, C. W. Wang, F. Y. Liu and W. L. Wang, Formation mechanism of methanesulfonic acid and ammonia clusters: A kinetics simulation study, *Atmos. Environ.*, 2020, **222**, 117161.

116 M. van Pinxteren, B. Fiedler, D. van Pinxteren, Y. Iinuma, A. Kortzinger and H. Herrmann, Chemical characterization of sub-micrometer aerosol particles in the tropical Atlantic Ocean: marine and biomass burning influences, *J. Atmos. Chem.*, 2015, **72**, 105–125.

117 C. Muller, Y. Iinuma, J. Karstensen, D. van Pinxteren, S. Lehmann, T. Gnauk and H. Herrmann, Seasonal variation of aliphatic amines in marine sub-micrometer particles at the Cape Verde islands, *Atmos. Chem. Phys.*, 2009, **9**, 9587–9597.

118 M. C. Facchini, S. Decesari, M. Rinaldi, C. Carbone, E. Finessi, M. Mircea, S. Fuzzi, F. Moretti, E. Tagliavini, D. Ceburnis and C. D. O'Dowd, Important source of marine secondary organic aerosol from biogenic amines, *Environ. Sci. Technol.*, 2008, **42**, 9116–9121.

119 X. F. Huang, C. R. Deng, G. S. Zhuang, J. Lin and M. X. Xiao, Quantitative analysis of aliphatic amines in urban aerosols based on online derivatization and high performance liquid chromatography, *Environ. Sci.: Processes Impacts*, 2016, **18**, 796–801.

120 H. Feng, X. N. Ye, Y. X. Liu, Z. K. Wang, T. X. Gao, A. Y. Cheng, X. F. Wang and J. M. Chen, Simultaneous determination of nine atmospheric amines and six inorganic ions by non-suppressed ion chromatography using acetonitrile and 18-crown-6 as eluent additive, *J. Chromatogr. A*, 2020, **1624**, 461234.

121 M. Wang, Q. Y. Wang, S. S. H. Ho, H. Li, R. J. Zhang, W. K. Ran, L. L. Qu, S. C. Lee and J. J. Cao, Chemical characteristics and sources of nitrogen-containing organic compounds at a regional site in the North China Plain during the transition period of autumn and winter, *Sci. Total Environ*, 2022, **812**, 151451.

122 A. P. Sullivan, K. B. Benedict, C. M. Carrico, M. K. Dubey, B. A. Schichtel and J. C. Collett, A quantitative method to measure and speciate amines in ambient aerosol samples, *Atmosphere*, 2020, **11**, 808.

123 Q. Zhang and C. Anastasio, Free and combined amino compounds in atmospheric fine particles (PM2.5) and fog waters from Northern California, *Atmos. Environ.*, 2003, **37**, 2247–2258.

124 Z. Y. Liu, M. Li, X. F. Wang, Y. H. Liang, Y. R. Jiang, J. Chen, J. S. Mu, Y. J. Zhu, H. Meng, L. X. Yang, K. Y. Hou, Y. F. Wang and L. K. Xue, Large contributions of anthropogenic sources to amines in fine particles at a coastal area in northern China in winter, *Sci. Total Environ*, 2022, **839**, 156281.

125 B. K. Place, A. T. Quilty, R. A. Di Lorenzo, S. E. Ziegler and T. C. VandenBoer, Quantitation of 11 alkylamines in atmospheric samples: separating structural isomers by ion chromatography, *Atmos. Meas. Tech.*, 2017, **10**, 1061–1078.

126 K. Gorzelska and J. N. Galloway, Amine nitrogen in the atmospheric environment over the north Atlantic ocean, *Global Biogeochem. Cycles*, 1990, **4**, 309–333.

127 V. M. Kerminen, X. Chen, V. Vakkari, T. Petaja, M. Kulmala and F. Bianchi, Atmospheric new particle formation and growth: review of field observations, *Environ. Res. Lett.*, 2018, **13**, 103003.

128 U. Poschl, Atmospheric aerosols: Composition, transformation, climate and health effects, *Angew. Chem., Int. Ed.*, 2005, **44**, 7520–7540.

129 IPCC, in *Climate Change 2021: The Physical Science Basis. Contribution of Working Group I to the Sixth Assessment Report of the Intergovernmental Panel on Climate Change*, ed. V. Masson-Delmotte, United Kindom and New York, NY, USA, 2021, p. 2391.

130 A. L. Hodshire, P. Campuzano-Jost, J. K. Kodros, B. Croft, B. A. Nault, J. C. Schroder, J. L. Jimenez and J. R. Pierce, The potential role of methanesulfonic acid (MSA) in aerosol formation and growth and the associated radiative forcings, *Atmos. Chem. Phys.*, 2019, **19**, 3137–3160.

131 C. A. Pope and D. W. Dockery, Health effects of fine particulate air pollution: Lines that connect, *J. Air Waste Manage. Assoc.*, 2006, **56**, 709–742.

132 M. R. Heal, P. Kumar and R. M. Harrison, Particles, air quality, policy and health, *Chem. Soc. Rev.*, 2012, **41**, 6606–6630.

133 J. Lelieveld, Clean air in the Anthropocene, *Faraday Discuss.*, 2017, **200**, 693–703.

134 J. Lelieveld, J. S. Evans, M. Fnais, D. Giannadaki and A. Pozzer, The contribution of outdoor air pollution sources to premature mortality on a global scale, *Nature*, 2015, **525**, 367–371.

135 A. L. Moreno-Ríos, L. P. Tejeda-Benítez and C. F. Bustillo-Lecompte, Sources, characteristics, toxicity, and control of ultrafine particles: An overview, *Geosci Front.*, 2022, **13**, 101147.

136 S. W. Sang, C. Chu, T. C. Zhang, H. Chen and X. R. Yang, The global burden of disease attributable to ambient fine particulate matter in 204 countries and territories, 1990–2019: A systematic analysis of the Global Burden of Disease Study 2019, *Ecotoxicol. Environ. Saf.*, 2022, **238**, 113588.

137 X. J. Deng, X. X. Tie, D. Wu, X. J. Zhou, X. Y. Bi, H. B. Tan, F. Li and C. L. Hang, Long-term trend of visibility and its characterizations in the Pearl River Delta (PRD) region, China, *Atmos. Environ.*, 2008, **42**, 1424–1435.

138 D. Chang, Y. Song and B. Liu, Visibility trends in six megacities in China 1973–2007, *Atmos. Res.*, 2009, **94**, 161–167.

139 A. Singh, W. J. Bloss and F. D. Pope, 60 years of UK visibility measurements: impact of meteorology and atmospheric pollutants on visibility, *Atmos. Chem. Phys.*, 2017, **17**, 2085–2101.

140 J. G. Watson, Visibility: science and regulation, *J. Air Waste Manage. Assoc.*, 2002, **52**, 628–713.

141 A. L. Moreno-Rios, L. P. Tejeda-Benitez and C. F. Bustillo-Lecompte, Sources, characteristics, toxicity, and control of ultrafine particles: An overview, *Geosci Front.*, 2022, **13**, 101147.

142 M. J. Ezell, H. Chen, K. D. Arquero and B. J. Finlayson-Pitts, Aerosol fast flow reactor for laboratory studies of new particle formation, *J. Aerosol Sci.*, 2014, **78**, 30–40.

143 J. N. Smith, K. F. Moore, P. H. McMurry and F. L. Eisele, Atmospheric measurements of sub-20 nm diameter particle chemical composition by thermal desorption chemical ionization mass spectrometry, *Aerosol Sci. Technol.*, 2004, **38**, 100–110.

144 D. Voisin, J. N. Smith, H. Sakurai, P. H. McMurry and F. L. Eisele, Thermal desorption chemical ionization mass spectrometer for ultrafine particle chemical composition, *Aerosol Sci. Technol.*, 2003, **37**, 471–475.

145 M. J. Lawler, P. M. Winkler, J. Kim, L. Ahlm, J. Trostl, A. P. Praplan, S. Schobesberger, A. Kuerten, J. Kirkby, F. Bianchi, J. Duplissy, A. Hansel, T. Jokinen, H. Keskinen, K. Lehtipalo, M. Leiminger, T. Petaja, M. Rissanen, L. Rondo, M. Simon, M. Sipila, C. Williamson, D. Wimmer, I. Riipinen, A. Virtanen and J. N. Smith, Unexpectedly acidic nanoparticles formed in dimethylamine-ammonia-sulfuric-acid nucleation experiments at CLOUD, *Atmos. Chem. Phys.*, 2016, **16**, 13601–13618.

146 H. Chen, S. Chee, M. J. Lawler, K. C. Barsanti, B. M. Wong and J. N. Smith, Size resolved chemical composition of nanoparticles from reactions of sulfuric acid with ammonia and dimethylamine, *Aerosol Sci. Technol.*, 2018, **52**, 1120–1133.

147 D.-R. Chen and D. Y. Pui, A high efficiency, high throughput unipolar aerosol charger for nanoparticles, *J. Nanopart. Res.*, 1999, **1**, 115–126.

148 P. H. McMurry, A. Ghimire, H.-K. Ahn, H. Sakurai, K. Moore, M. Stolzenburg and J. N. Smith, Sampling nanoparticles for chemical analysis by low resolution electrical mobility classification, *Environ. Sci. Technol.*, 2009, **43**, 4653–4658.

149 D. V. Davis and R. G. Cooks, Site of protonation and bifunctional group-interactions in a,w-hydroxyalkylamines, *Org. Mass Spectrom*, 1981, **16**, 176–179.

150 G. Bouchoux, N. Choret, F. Berruyer-Penaud and R. Flammang, Thermochemistry and unimolecular reactivity of protonated alpha,omega-aminoalcohols in the gas phase, *Int. J. Mass Spectrom.*, 2002, **217**, 195–230.

151 E. P. L. Hunter and S. G. Lias, Evaluated gas phase basicities and proton affinities of molecules: An update, *J. Phys. Chem. Ref. Data*, 1998, **27**, 413–656.

152 S. Kapteina, K. Slowik, S. P. Verevkin and A. Heintz, Vapor pressures and vaporization enthalpies of a series of ethanolamines, *J. Chem. Eng. Data*, 2005, **50**, 398–402.

153 I. N. Tang and H. R. Munkelwitz, Determination of vapor-pressure from droplet evaporation kinetics, *J. Colloid Interface Sci.*, 1991, **141**, 109–118.

154 S.-L. von der Weiden, F. Drewnick and S. Borrmann, Particle loss calculator – A new software tool for the assessment of the performace of aerosol inlet systems, *Atmos. Meas. Tech.*, 2009, **2**, 469–494.

155 M. Kulmala, H. Vehkamäki, T. Petäjä, M. Dal Maso, A. Lauri, V. M. Kerminen, W. Birmili and P. H. McMurry, Formation and growth rates of ultrafine atmospheric particles: a review of observations, *J. Aerosol Sci.*, 2004, **35**, 143–176.

156 T. L. Greaves, A. Weerawardena, C. Fong, I. Krodkiewska and C. J. Drummond, Protic ionic liquids: Solvents with tunable phase behavior and physicoschemical properties, *J. Phys. Chem. B*, 2006, **110**, 22479–22487.

157 G. Cai, S. Yang, Q. Zhou, L. Liu, J. Xu and S. Zhang, Physicochemical properties of various 2-hydroxyethylammonium sulfonate-based protic ionic liquids and their potential application in hydrodeoxygenation, *Front. Chem.*, 2019, **7**, 196.

158 X. Lu, J. M. Vincent-Luna, S. Calero, M. Roldan-Ruiz, R. Jimenez, M. L. Ferrer, M. C. Gutierrez and F. del Monte, Aqueous co-solvent in zwitterionic-based protic ionic liquids as electrolytes in 2.0 V supercapacitors, *ChemSusChem*, 2020, **13**, 5983–5995.

159 S. J. Brown, D. Yalcin, S. Pnadiancherri, T. C. Le, I. O'rhan, K. Hearn, Q. Han, C. J. Drummond and T. L. Greaves, Characterising a protic ionic liquid library with applied machine learning algorithms, *J. Mol. Liq.*, 2022, **367**, 120453.

160 R. McGraw and A. Laaksonen, Scaling properties of the critical nucleus in classical and molecular-based theories of vapor-liquid nucleation, *Phys. Rev. Lett.*, 1996, **76**, 2754–2757.

161 O. Kupiainen-Maatta, T. Olenius, H. Korhonen, J. Malilal, M. Dal Maso, K. Lehtinen and H. Vehkamaki, Critical cluster size cannot in pracctice be determined by slope analysis in atmospherically relevant applications, *J. Aerosol Sci.*, 2014, **77**, 127–144.

162 Y. Liu, H. B. Xie, F. F. Ma, J. W. Chen and J. Elm, Amine-enhanced methanesulfonic acid driven nucleation: Predictive model and cluster formation mechanism, *Environ. Sci. Technol.*, 2022, **56**, 7751–7760.

163 J. Xu, V. Perraud, B. J. Finlayson-Pitts and R. B. Gerber, Uptake of water by an acid-base nanoparticle: theoretical and experimental studies of the methanesulfonic acid-methylamine system, *Phys. Chem. Chem. Phys.*, 2018, **20**, 22249–22259.

164 V. Perraud, J. R. Horne, A. S. Martinez, J. Kalinowski, S. Meinardi, M. L. Dawson, L. M. Wingen, D. Dabdub, D. R. Blake, R. B. Gerber and B. J. Finlayson-Pitts, The future of airborne sulfur-containing particles in the absence of fossil fuel sulfur dioxide emissions, *Proc. Natl. Acad. Sci. U. S. A.*, 2015, **112**, 13514–13519.

165 J. G. Murphy, P. K. Gregoire, A. G. Tevlin, G. R. Wentworth, R. A. Ellis, M. Z. Markovic and T. C. VandenBoer, Observational constraints on particle acidity using measurements and modelling of particles and gases, *Faraday Discuss.*, 2017, **200**, 379–395.

166 Z. Klimont, S. J. Smith and J. Cofala, The last decade of global anthropogenic sulfur dioxide: 2000-2011 emissions, *Environ. Res. Lett.*, 2013, **8**, 1–6.

167 T. J. Breider, L. J. Mickley, D. J. Jacob, C. Ge, J. Wang, M. P. Sulprizio, B. Croft, D. A. Ridley, J. R. McConnell, S. Sharma, L. Husain, V. A. Dutkiewicz, K. Eleftheriadis, H. Skov and P. K. Hopke, Multidecadal trends in aerosol radiative forcing over the Arctic: Contribution of changes in anthropogenic aerosol to Arctic warming since 1980, *J. Geophys. Res.*, 2017, **122**, 3573–3594.

168 G. M. Hidy and C. L. Blanchard, The changing face of lower tropospheric sulfur oxides in the United States, *Elem. Sci. Anth.*, 2016, **4**, 000138.
169 D. I. Stern, Global sulfur emissions from 1850 to 2000, *Chemosphere*, 2005, **58**, 163–175.
170 M. Amann, Z. Klimont and F. Wagner, Regional and global emissions of air pollutants: Recent trends and future scenarios, *Ann. Rev. Environ. Resour.*, 2013, **38**, 31–55.
171 P. K. Quinn, G. Shaw, E. Andrews, E. G. Dutton, T. Ruoho-Airola and S. L. Gong, Arctic haze: current trends and knowledge gaps, *Tellus B*, 2007, **59**, 99–114.
172 D. Hirdman, J. F. Burkhart, H. Sodemann, S. Eckhardt, A. Jefferson, P. K. Quinn, S. Sharma, J. Strom and A. Stohl, Long-term trends of black carbon and sulphate aerosol in the Arctic: changes in atmospheric transport and source region emissions, *Atmos. Chem. Phys.*, 2010, **10**, 9351–9368.

Electronic Supplementary Material (ESI) for Physical Chemistry Chemical Physics.

Electronic Supplementary Information for

Implications for New Particle Formation in Air of the Use of Monoethanolamine in Carbon Capture and Storage

Véronique Perraud,* Kanuri Roundtree, Patricia M. Morris, James N. Smith* and Barbara J. Finlayson-Pitts

The supporting information (26 pages) contains text covering additional details on the experimental methods as well as 15 figures (S1-S15).

Flow reactor diagram

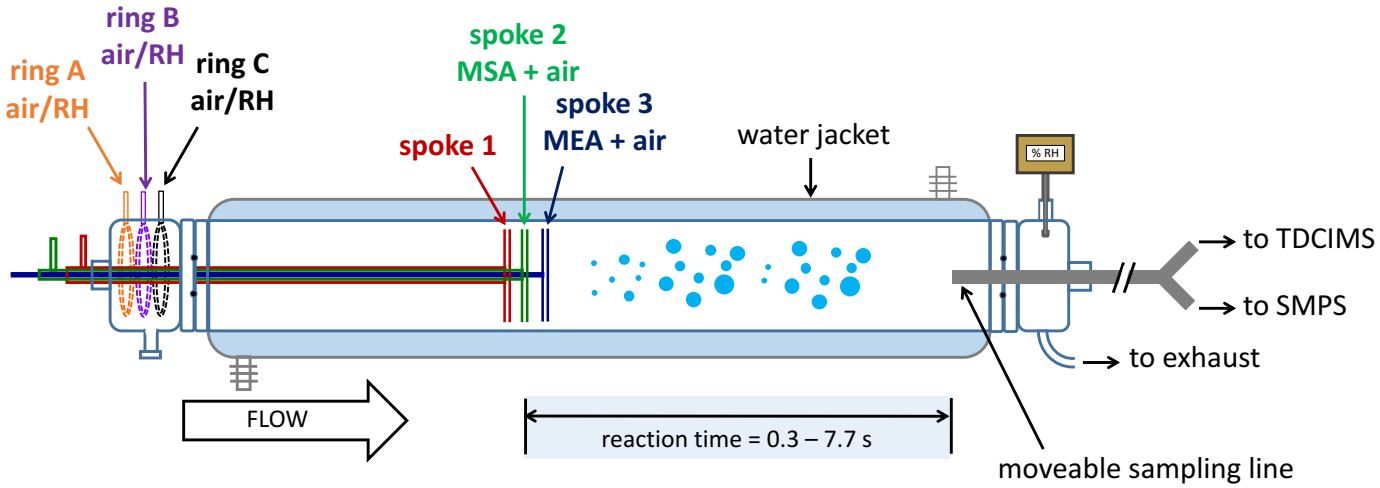

Figure S1. Diagram of the 1-m borosilicate flow reactor (adapted from Perraud et al.[1]) for the MSA+MEA experiments. Flows were distributed as follows: ring A, 4.3 or 8.5 L min^{-1} (either dry or humidified air); ring B, 4.2 or 8.5 L min^{-1} (either dry or humidified air); ring C, 0 or 4.3 L min^{-1} (either dry or humidified air); spoke 1 had no flow; spoke 2, ~1 L min^{-1} (mixture of MSA flow and clean air); spoke 3, ~1 L min^{-1} (mixture of MEA flow and clean air). All the flows were controlled by high-precision mass flow controllers (Alicat or MKS) and were checked with a flow meter (Sensidyne; Gilibrator 2) periodically. The reaction times at which measurements were taken ranged from 0.5 to 7.7 s (total flow ~10.7 L min^{-1}) or 0.3 to 4.5 s (total flow ~23.4 L min^{-1}).

Text S1. Gas phase reactant concentration determination.

(a) MSA sampling and analysis: The flow of gas phase MSA exiting the trap (53, 107, or 216 ccm) was sampled through a 33 mm diameter Durapore filter (Millex-HV, 0.45 μm pore size) for 10 min. Immediately after sampling, the filter was extracted using 10 mL of nanopure water and the extract was stored at room temperature prior to analysis by UPLC-ESI-MS(-). Each measurement was carried out in triplicate. For each sample, a 5 μL aliquot was analyzed using an UPLC-PDA-MS platform (Waters) equipped with an Acquity UPLC system (including a quaternary pump, an autosampler, a column manager and a photodiode array detector) coupled to a Xevo TQD triple quadrupole mass spectrometer. An Aquity UPLC BEH C18 column (2.1 x 50 mm, 1.7 μm thickness; Waters) fitted with a BEH C18 (2.1 x 5.0 mm; Waters) guard column maintained at 50°C was used for the separation. The isocratic mobile phase (400 μL min^{-1}) was composed of 95% of a 0.2% acetic acid (Optima, LC-MS grade, Fisher) aqueous solution (18.2 MΩ-cm nanopure water) combined with 5% LC-MS grade methanol (Optima, Fisher). The sample exiting the analytical column was introduced into the mass spectrometer using an electrospray ionization source (ESI) set in negative ion mode, with the following parameters: capillary voltage, 2.0 kV; cone voltage, 40 V; desolvation temperature, 500°C, desolvation gas flow rate, 1000 L hr^{-1}; source temperature, 120°C. The analysis was performed using a multiple reaction monitoring (MRM) method following the m/z 95 ($CH_3SO_3^-$) => 80 (SO_3^-) transition that is specific to MSA, with a collision energy of 16 eV. The data were acquired using MassLynx (Waters) and processed using TargetLynx (Waters).

(b) MEA/MA sampling and analysis: The flow of gas phase amine (MEA or MA) exiting the trap was sampled using custom-built cation exchange resin cartridges[2] for 20 or 40 min. Prior to the first sampling, the cartridges were first cleaned and conditioned by flushing them ten times with the extraction solution which is a 50 mM oxalic acid solution in nanopure water. The solution was prepared daily by dissolving 9 g of oxalic acid (Sigma Aldrich, 98%) into 2 L of nanopure water. Immediately after sampling, the cartridges were extracted sequentially three times with 10 mL of the extraction solution. The three extracts were collected and analyzed separately. The amines were mostly present in the first extract (recovery 93-100%) but the additional extractions were performed to ensure full recovery and to ensure the cartridge was clean for the next sampling. The extracts (injection volume 25 uL) were analyzed using a Dionex IC1100 (ThermoScientific) ion chromatography system equipped with a CERS500 4 mm suppressor and a Dionex GC16 (5 x 50 mm) guard column coupled to an IonPac CS16 (5 x 25 mm) analytical column. The separation of the amines was achieved using an isocratic eluent composed of a 50 mM oxalic acid in nanopure water with a flow rate of 1 mL min^{-1}, and a column temperature maintained at 40°C. The amines were detected by conductimetry.

Calibration curves for MEA and MA were obtained using monoethanolamine hydrochloride (MEA-HCl; Sigma Aldrich, > 99.0%) and methylamine hydrochloride (MA-HCl; Aldrich; >98%) standard solutions in water, respectively. Data were acquired using Chromeleon (ThermoScientific, version 7.2.10). An example of a chromatogram obtained from a cartridge extract is presented in Fig. S2 and shows no additional measurable ammonia in the extract compared to the blank cartridge. The gas phase concentration of MEA was determined to be 164 ± 19 ppb out of the trap (n = 22; one standard variation), while the concentration of MA was 1.2 ± 0.2 ppm (n = 9; one standard variation).

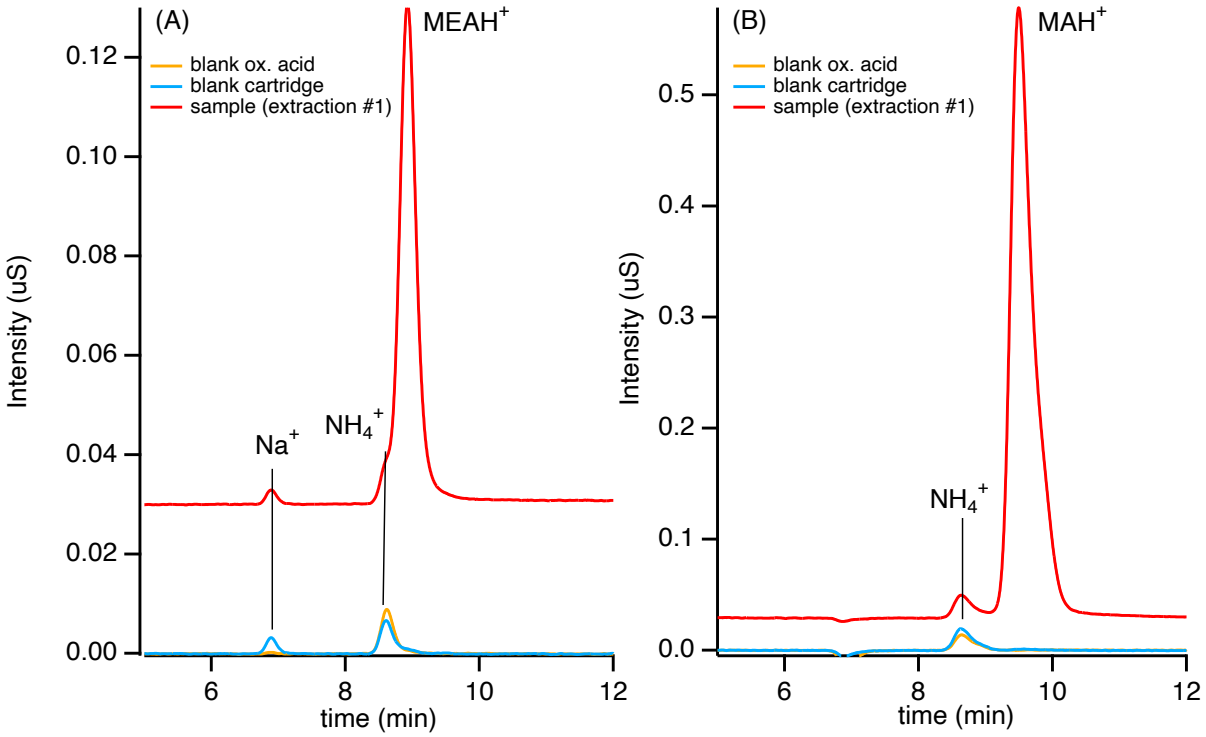

Figure S2. IC chromatograms of a cartridge extract (red trace) compared to a blank cartridge (blue trace) and the extraction solution (50 mM oxalic acid in nanopore water; orange trace) taken from (A) the MEA trap and (B) for the MA trap. The ammonia present in the extract originates from small amounts of ammonia present in the extraction solution.

Text S2. Particle transmission determination

The total particle transmission efficiency through the sampling lines as a function of particle diameter (Fig. S3) were determined using a combination of measurements and simulation. Exiting the flow tube reactor, the particles first traveled through a 142 cm long straight stainless steel sampling line (0.64 cm O. D.). This tube is moved along the centerline of the FT to vary reaction times. The total flow rate through the sampling line was either 3.5 L min^{-1} or 4.8 L min^{-1} corresponding to the sum of the scanning mobility particle sizer (SMPS, 1.5L min^{-1}) and the TDCIMS flows (either 2.0 L min^{-1} or 3.3 L min^{-1}). The particle transmission efficiency through this sampling line was estimated using the particle loss calculator tool developed by von

der Weinder et al.[3] using a density of 1 g cm^{-3} and, the loss was calculated to be minimal for particles with diameter larger than 4 nm (> 80% particle transmission; red trace). The end of the sampling line was terminated by a y-shaped connector to split the flows between the TDCIMS and the SMPS. Sampling from the y-connector to the SMPS was initially conducted using a 117 cm long flexible stainless steel bellows attached to the FT sampling line. As described below, the rough walls of the bellows resulted in significant particle loss and was later replaced with a smooth bore 84 cm long aluminum tube. Comparing the two size distributions, a drastic loss of nanoparticles was observed when the bellows were used, and particle loss was experimentally determined by taking the ratio of particle concentrations measurements using the bellows to the particle concentrations measured with the straight shorter aluminum line (blue squares). To assess the total particle transmission efficiency through the entire sampling line from the FT to the inlet of the SMPS, the particle loss calculator was first used to estimate the losses through the FT sampling line (red trace) and then through the smooth bore aluminum line (green trace) connecting the sampling line to the SMPS. The total particle transmission efficiency through the sampling lines from the FT to the inlet of SMPS was then defined as the product of all individual particle transmission efficiencies (black trace). For example, as illustrated in Fig. S4, for a particle diameter of 6 nm, the particle transmissions are 0.88 (FT sampling lines), 0.86 (aluminum smooth bore line) and 0.44 (correction from bellows to aluminum line) respectively for a TDCIMS inlet flow of 2.0 L min^{-1}, yielding a total particle transmission efficiency through the entire sampling line of $0.88 \times 0.86 \times 0.44 = 0.33$. Subsequently, all results presented in this work have been normalized for the total particle transmission efficiency.

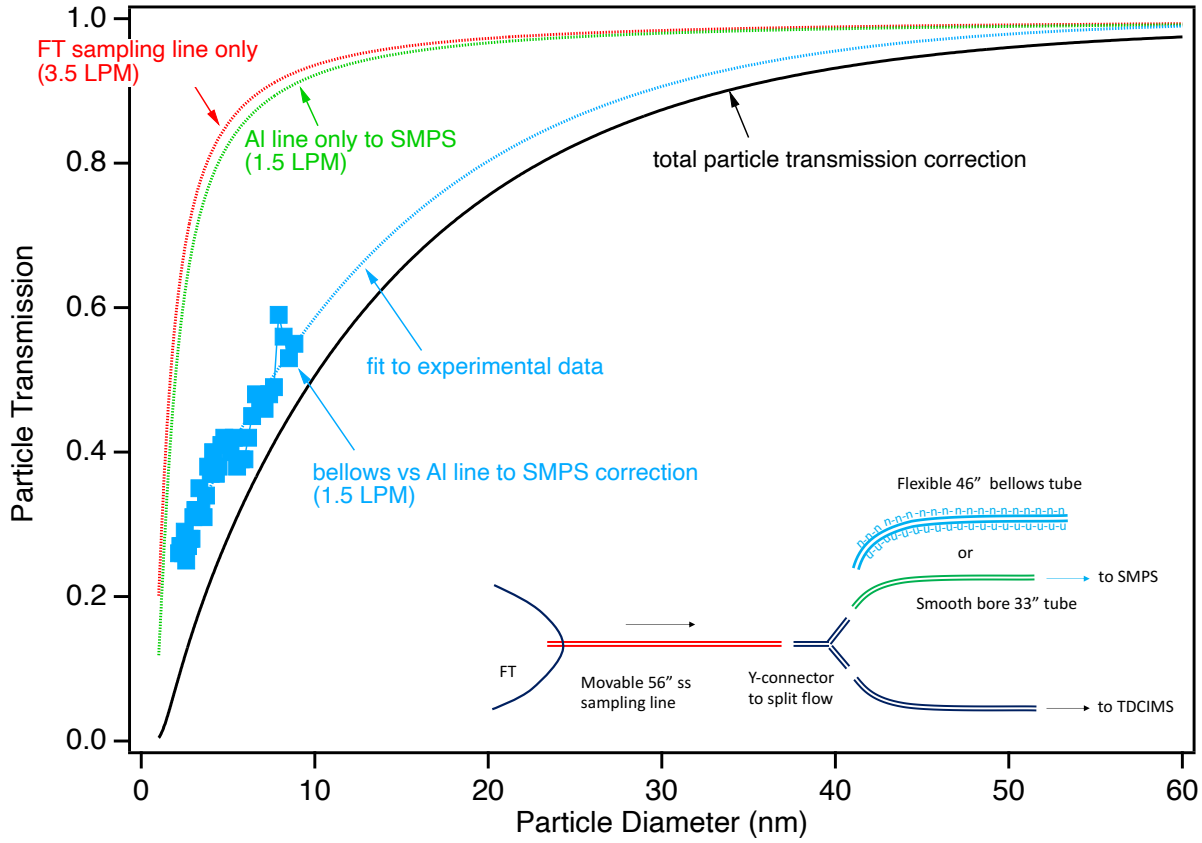

Figure S3. Example of determination of the particle transmission through the sampling lines to the SMPS inlet for a TDCIMS inlet flow of 2.0 L min^{-1}. Red and green lines represent simulated[3] particle transmission through the flow tube sampling line (3.5 L min^{-1}) and through the aluminum smooth bore line to the SMPS (1.5 L min^{-1}), respectively. Blue squared data points correspond to experimentally determined particle transmission correction (bellows vs aluminum line to the SMPS, 1.5 L min^{-1}). The blue line corresponds to the fit to the experimental data. The black line represents the final total particle transmission through the sampling line train to the SMPS accounting for all corrections. (LPM corresponds to L min^{-1}; ss, stainless steel)

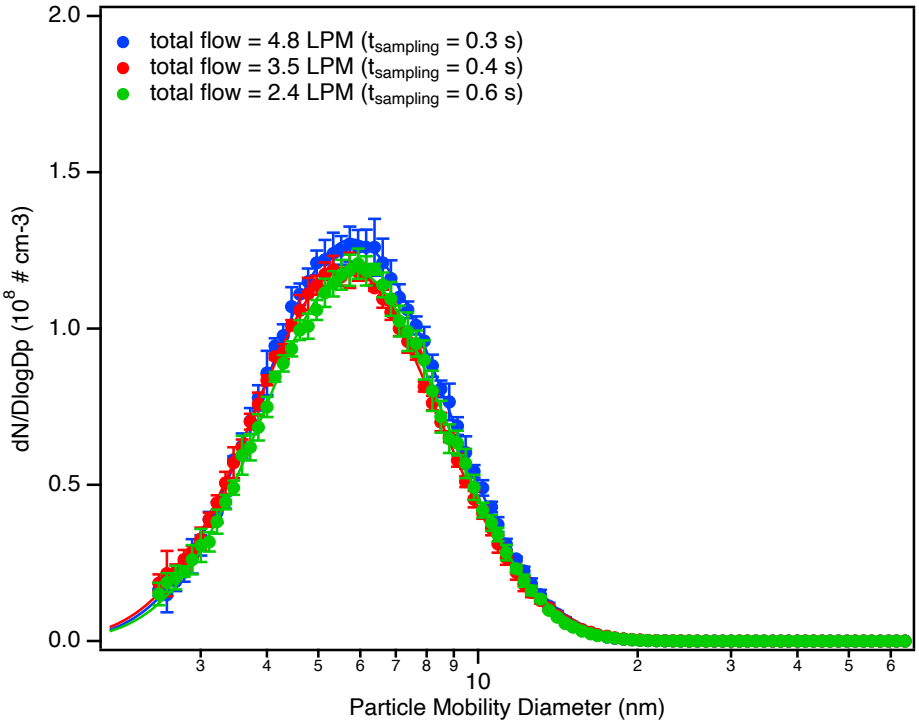

Figure S4. Size distributions of particles measured by the SMPS for the MSA (6.1 ppb) + MEA (3.3 ppb) reaction at different flow rates and residence times in the sampling line. All measurements were conducted at 0.5 s reaction time under dry conditions, but a similar result was obtained for all reaction times. Size distributions are all corrected for particle losses through the sampling lines (see Text S2 above). $t_{sampling}$ refers to the extra residence time the particles have in the flow tube sampling line, over and above the reaction time in the flow tube.

Stability of the size distributions measured from the MSA+MEA system

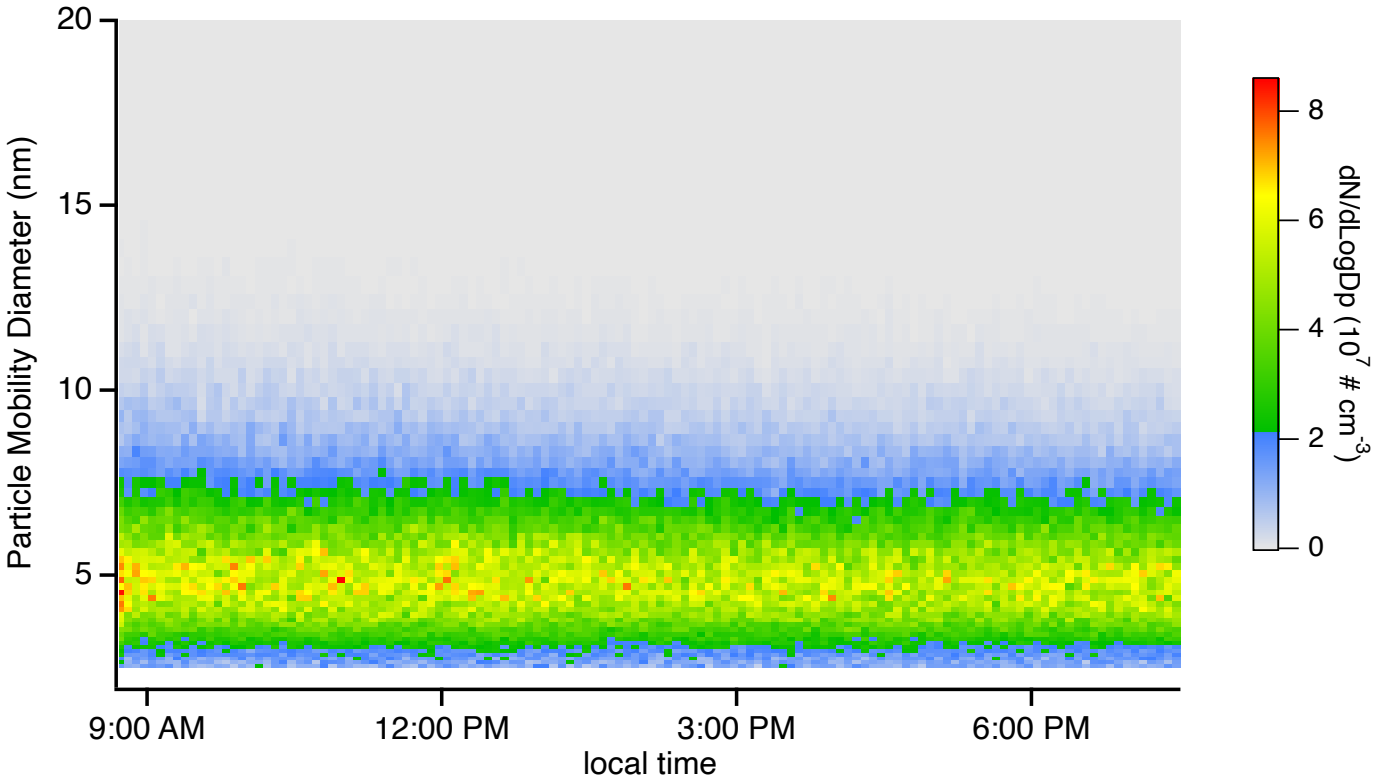

Figure S5. Stability of the size distribution of particles measured by the SMPS for the MSA (0.68 ppb) + MEA (1.4 ppb) reaction system. The measurement was conducted at 4.5 s reaction time under dry condition. Size distributions are corrected for particle losses through the sampling lines (see Text S2 above).

Details of the TDCIMS analysis

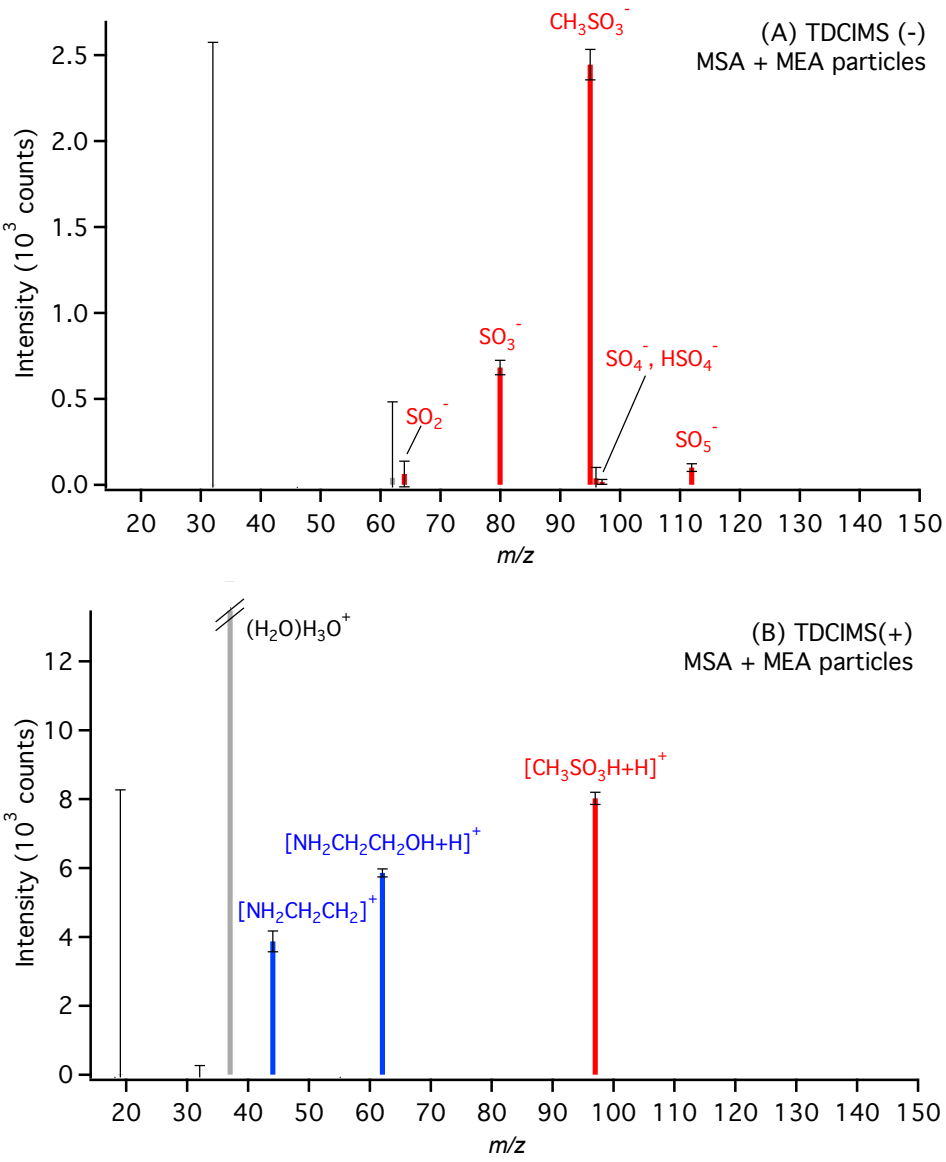

Figure S6. Representative mass spectra of ion abundance observed for MSA-MEA particles collected at 4.5 s reaction time in (A) negative ion mode and (B) positive ion mode (volume mean diameter 6.8 nm; collection time, 120 s; [MSA] =0.68 ppb; [MEA] = 1.5 ppb). The red traces correspond to ions observed for MSA while the blue traces are for MEA. Note these are not raw MS spectra, but rather they represent the distribution of the ions observed for each species (i.e. all the other ions have been omitted for clarity). The observed MS spectra were not dependent on the reactant concentrations (i.e. the same ions were observed for all [MSA] concentrations investigated), but the signal intensity measured for each ion was proportional to the mass of nanoparticle collected. The grey bars represent the reagent ions.

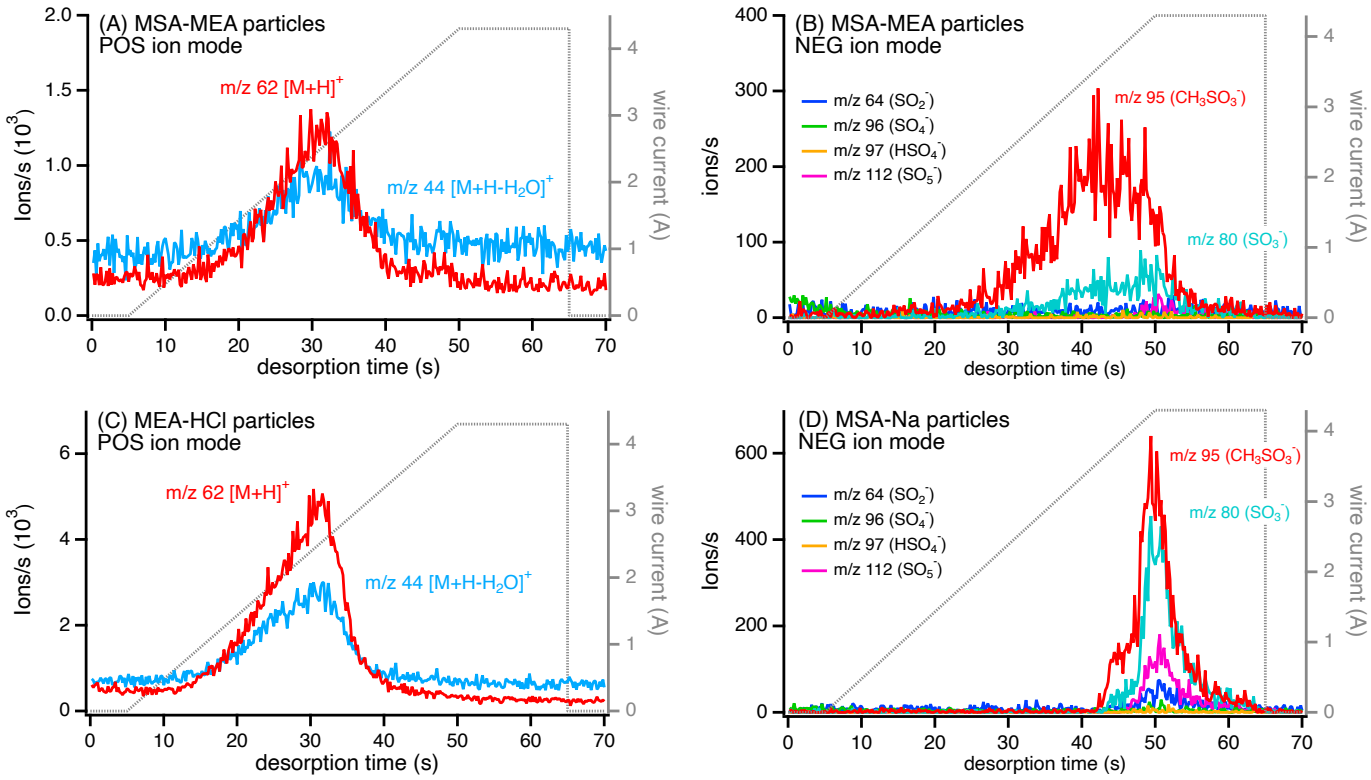

Figure S7. Representative ion desorption profiles for (A) MEA and (B) MSA present in 6 nm MSA-MEA particles collected from the flow reactor (collection time = 120 s), (C) MEA present in 15 nm atomized MEA-HCl particles (collection time = 240 s) and (D) MSA present in 15 nm atomized MSA-Na particles (collection time = 240 s). In all graphs, the grey line corresponds to the wire current.

Text S3. TDCIMS analysis cycle description: The TDCIMS method has been described in detail previously.[1,4-6] Briefly, sampled particles were charged and size-selected using two unipolar chargers and radial differential mobility analyzers operating in parallel. Particles were then electrostatically collected on a Pt wire by the application of a DC voltage of 3.5 kV. After collection for 10-1200 sec, the Pt wire was translated into the ion source where it was resistively heated by the application of a power-controlled AC current from room temperature to an estimated temperature of ~600°C for a duration of 70 s (corresponding to a wire current of 4.30

A) to desorb the particle components. The desorbed species were then ionized via chemical ionization using ions generated by a radioactive source (^{210}Po; NRD). Following ionization, each species was analyzed by a high-resolution time-of-flight mass analyzer (TOF mass analyzer, Tofwerk AG). Prior to each measurement, the wire was resistively heated at the maximum wire current of 4.30 A for 30 s to clean any residue left on the wire, followed by a cool down step (~30 s) to room temperature. Each collection cycle (cleaning/cooldown/ collection/analysis) was followed by a background cycle during which no collection voltage was applied to the Pt wire.

Text S4. Determination of the TDCIMS collection efficiency. An "exhaust SMPS" consisting of a ^{210}Po bipolar neutralizer, a nano-differential mobility diameter (nano-DMA; model 3085, TSI, Inc.) and an ultrafine condensation particle counter (UCPC; model 3776, TSI, Inc.) was used to detect the particles downstream of the TDCIMS inlet. The ^{210}Po bipolar neutralizer used in these studies was developed by the Particle Technology Lab (PTL) at the University of Minnesota as described in Jiang et al.[7] The exhaust SMPS measured the size distribution over the mobility range of 2.5 to 24 nm using a recirculating sheath air flow rate of 10 L min^{-1} and an aerosol flow rate of 1.5 L min^{-1}. This was used to determine the particle mean volume diameter of the collected particles, which is calculated by taking the difference between the distribution of the particles during background (i.e. when no voltage is applied to the Pt wire) and that of the particles during collection, and estimating the volume mean diameter (Fig. S8). A second UCPC (model 3025; TSI Inc.) located again downstream of the collection wire was used to determine the total particle concentration collected from the difference in concentration during background and collection runs; this measurement was used to assess the size-dependent collection efficiency of the TDCIMS for each diameter selected (Fig. S9).

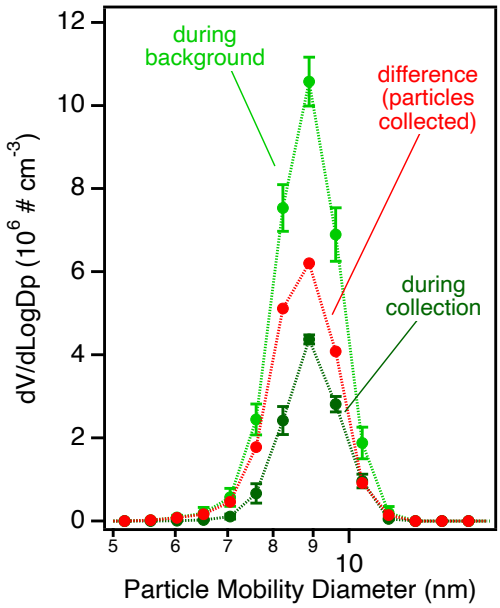

Figure S8. Example of a volume-based size distribution of MSA-MEA particles taken by the "exhaust" SMPS (i.e. detecting particles that are not collected by the Pt wire) for rDMA voltage = 110V (corresponding to a measured volume-based mean mobility diameter of 9 nm). The experimental data correspond to averages of at least two scans (error bars represent one standard deviation).

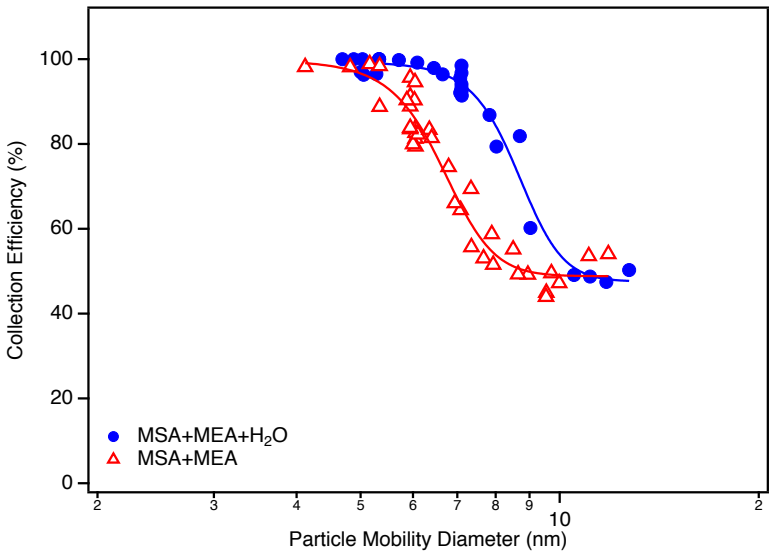

Figure S9. Experimentally determined TDCIMS collection efficiency for the MSA+MEA system (dry conditions; red trace) and the MSA+MEA+H_2O system (52% RH; blue trace). The TDCIMS was operated in high resolution mode with 1 L min^{-1} inlet flow and 10 L min^{-1} sheath air flow for each radial inlet DMA. For each data point, the particle mobility diameter corresponds to a volume mean diameter measured with the exhaust SMPS.

Text S5. TDCIMS calibration and acid/base molar ratio determination. Three or four specific ions present in all mass spectra were chosen in each polarity to mass calibrate each spectrum. In negative ion mode, these calibration ions were *m/z* 31.99 (O_2^-, reagent ion) as well as Cl^- ion at *m/z* 34.97 and NO_3^- at *m/z* 61.99 that were always present in the background. In the positive ion mode, these calibration ions were *m/z* 19.02 (H_3O^+, reagent ion) as well as N_2H^+ at *m/z* 29.01, and two siloxane peaks present at *m/z* 297.08 $[(CH_3SiCH_3O)_4+H]^+$ and 371.10 $[(CH_3SiCH_3O)_5+H]^+$. From each acquired mass spectrum, the desorption profile (i.e. intensity as a function of desorption time) for each ion of interest is extracted (Fig. S7). The desorption profiles are then processed following these steps to obtain a total background-subtracted integrated signal for each ion of interest: (1) the signal intensity for each ion is scaled to the reagent ion on a point-to-point basis over the entire desorption profile, and corrected for baseline; (2) the signal intensity is then integrated over a defined period of the desorption time; (3) the signal intensities of each ion for one given species (MSA or MEA) are summed; (4) the signal is normalized to an average reagent ion signal ($I^{reference}$ = 1.9× 10^4 ions/s for O_2^- and 1.1× 10^5 ions/s for H_3O^+) measured during calibration to account for day-to-day variability; and lastly (5) the corrected integrated signal intensity measured during a clean air sample is subtracted from that obtained during a collection to account for any residual signal from the system to yield a total signal intensity for negative ion mode (MSA) and positive ion mode (MEA) as:

$$(NEG\ signal) = \left(\sum neg\ ions(MSA)^{sample} \times \frac{I_{O_2^-}^{sample}}{I_{O_2^-}^{reference}}\right) - \left(\sum neg\ ions(MSA)^{cleanair} \times \frac{I_{O_2^-}^{cleanair}}{I_{O_2^-}^{reference}}\right) \quad (1)$$

$$(POS\ signal) = \left(\sum pos\ ions(MEA)^{sample} \times \frac{I_{H_3O^+}^{sample}}{I_{H_3O^+}^{reference}}\right) - \left(\sum pos\ ions(MEA)^{cleanair} \times \frac{I_{H_3O^+}^{cleanair}}{I_{H_3O^+}^{reference}}\right) \quad (2)$$

The signal for each polarity is thus used to estimate the acid/base molar ratio using equation (3) below:

$$\frac{acid}{base} molar\ ratio = \frac{(NEG\ signal)}{(POS\ signal)} \times \frac{total\ vol.\ pos\ coll.(s)}{total\ vol.neg\ coll.(s)} \times \frac{1}{\left(\frac{acid}{base} calibration\right)} \quad (3)$$

where $\frac{acid}{base} calibration$ represent the calibrated acid/base molar ratio defined from an external calibration using reference particles as described below, and accounting for the total volume of particles collected (in cm^3) for each polarity as follows:

$$total\ vol.coll.(s) = \left(\frac{4}{3} \times \pi \times \left(\frac{d_{vol.}(nm)}{2} \times 10^{-7}\ \frac{cm}{nm}\right)^3\right) \times \left(N_{coll.} - N_{bkgd}\right) \times wire\ flow\ \left(\frac{cm^3}{s}\right) \times coll.time(s) \quad (4)$$

Where $d_{vol}(nm)$ is the volume-based mean mobility diameter, $N_{coll.}$ and N_{bkgd} are the total particle concentration measured with the UCPC located at the exhaust of the TDCIMS inlet region during a collection or a background (no voltage applied on the Pt wire) scan respectively.

To determine the relative ionization efficiency of MSA versus MEA, reference salt particles were generated using a constant output atomizer (TSI, Inc.; model 3076). Aqueous solutions of sodium methanesulfonate (MSA-Na; 98%; Aldrich) and monoethanolamine hydrochloride (MEA-HCl; ≥ 99%; Sigma Aldrich) were atomized separately using dry clean air (32 psi) as the carrier gas. The flow exiting the atomizer was 1.7 L min^{-1} and passed through a Nafion™ drier (FC125-240-5MP-02; PermaPure) with 10 L min^{-1} drying air followed by a diffusion drier containing molecular sieve (type 13X, Kurt J. Lesker and ACROS). The particles were neutralized using a ^{210}Po bipolar neutralizer (NRD LLC; model P-2021) before being diluted with an additional 3 to 5 L min^{-1} of dry clean air. Size distributions were measured using the SMPS operated in high flow mode with an aerosol flow rate of 1.5 L min^{-1} and a sheath air flow rate of 15 L min^{-1}. Typical representative size distributions for the atomized particles are

presented in Fig. S10. Particles were also sampled using the TDCIMS operating under high and low resolution to quantify MSA and MEA. For these measurements, particles with volume mean diameter ($d_{vol.}$) ranging from 15 to 17 nm were sampled. These were the smallest particles that could be sampled based on the size distribution generated. To estimate the total mass collected, the effective density (ρ_{eff}) for each set of particles was first determined using a tandem CPMA-SMPS approach.[8] Briefly, the atomized reference particles were first mass-selected using a centrifugal particle mass analyzer (CPMA, Cambustion, Ltd) and subsequently classified using the SMPS operating with a 0.3 L min^{-1} aerosol flow rate and either a 3 or a 15 L min^{-1} sheath air flow rate. Effective density (ρ_{eff}) for particles covering the range 20 – 200 nm were 1474 ± 13 kg m^{-3} for MSA-Na, 1136 ± 26 kg m^{-3} for MEA-HCl.[8] The total mass collected ($m_{coll.}$) was then derived as:

$$m_{part.}(\mu g) = \left(\frac{4}{3} \times \pi \times \left(\frac{d_{vol.}(nm)}{2} \times 10^{-7}\,\frac{cm}{nm}\right)^3\right) \times \left(\rho_{eff}\left(\frac{kg}{m^3}\right) \times 10^3\,\frac{g}{kg} \times 10^{-6}\,\frac{m^3}{cm^3}\right) \times 10^6\,\frac{\mu g}{g} \qquad (4)$$

$$m_{coll.}(pg) = m_{part.}(\mu g) \times \left(N_{coll.} - N_{bkgd}\right) \times wire\ flow\ \left(\frac{cm^3}{s}\right) \times coll.time(s) \times 10^6\,\frac{pg}{ug} \qquad (5)$$

The wire flow was comprised of the inlet flow (3.3 L min^{-1} or 2 L min^{-1}) and the ultrahigh purity nitrogen sheath air flow (1.25 L min^{-1}). Calibration curves for each species (Fig. S11) were plotted with the background-subtracted integrated signal as a function of the total number of moles collected:

$$(NEG\ ion\ signal) = slope(MSA) \times \left(\frac{m_{coll.}(MSANa)}{MW(MSANa)}\right) \qquad (6)$$

$$(POS\ ion\ signal) = slope(MEA) \times \left(\frac{m_{coll.}(MEAHCl)}{MW(MEAHCl)}\right) \qquad (7)$$

Thus, the

acid/base reference calibrated molar ratio can be defined as:

$$\frac{acid}{base}\,calibration = \frac{slope(MSA)}{slope(MEA)} \quad (8)$$

The slopes are for MSA 3.5×10^{17} counts mole^{-1}, and for MEA 3.9×10^{17} counts mole^{-1}, yielding a reference molar ratio of 0.89.

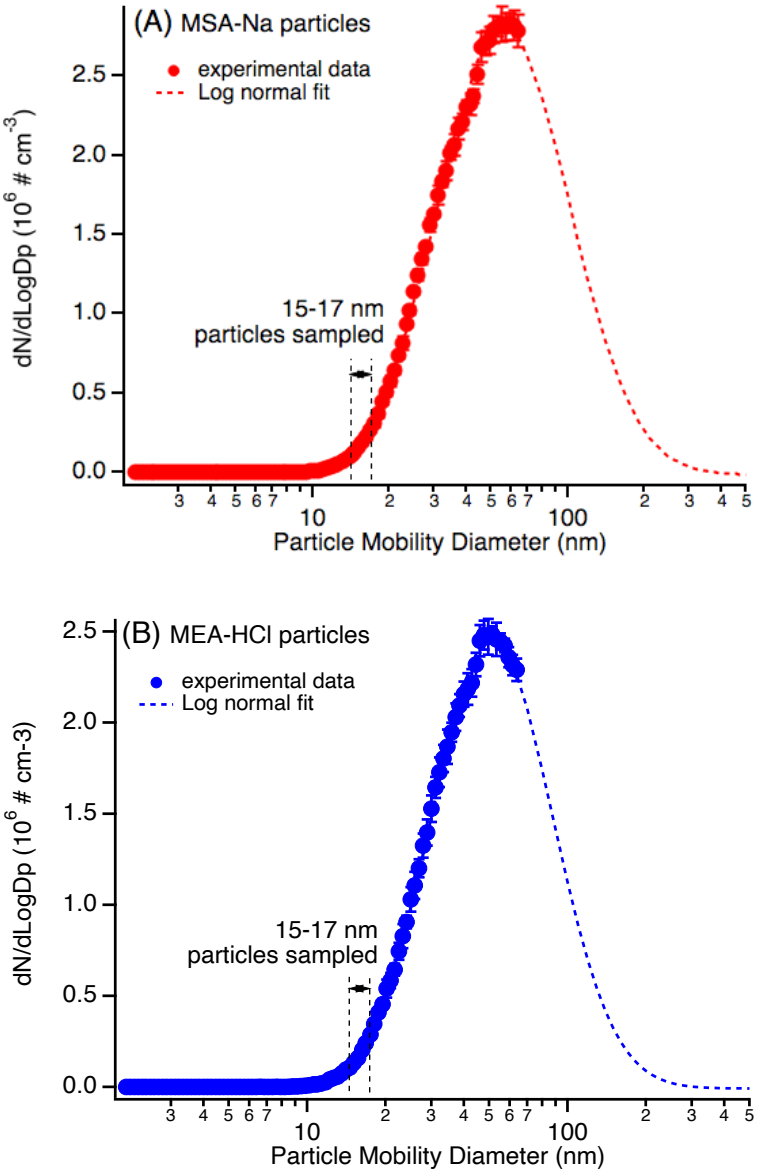

Figure S10. Typical size distributions of (A) MSA-Na and (B) MEA-HCl atomized reference particles. The SMPS was operated with an aerosol flow rate of 1.5 L min^{-1} and a sheath air flow rate of 15 L min^{-1}, resulting in a maximum mobility diameter of 64 nm.

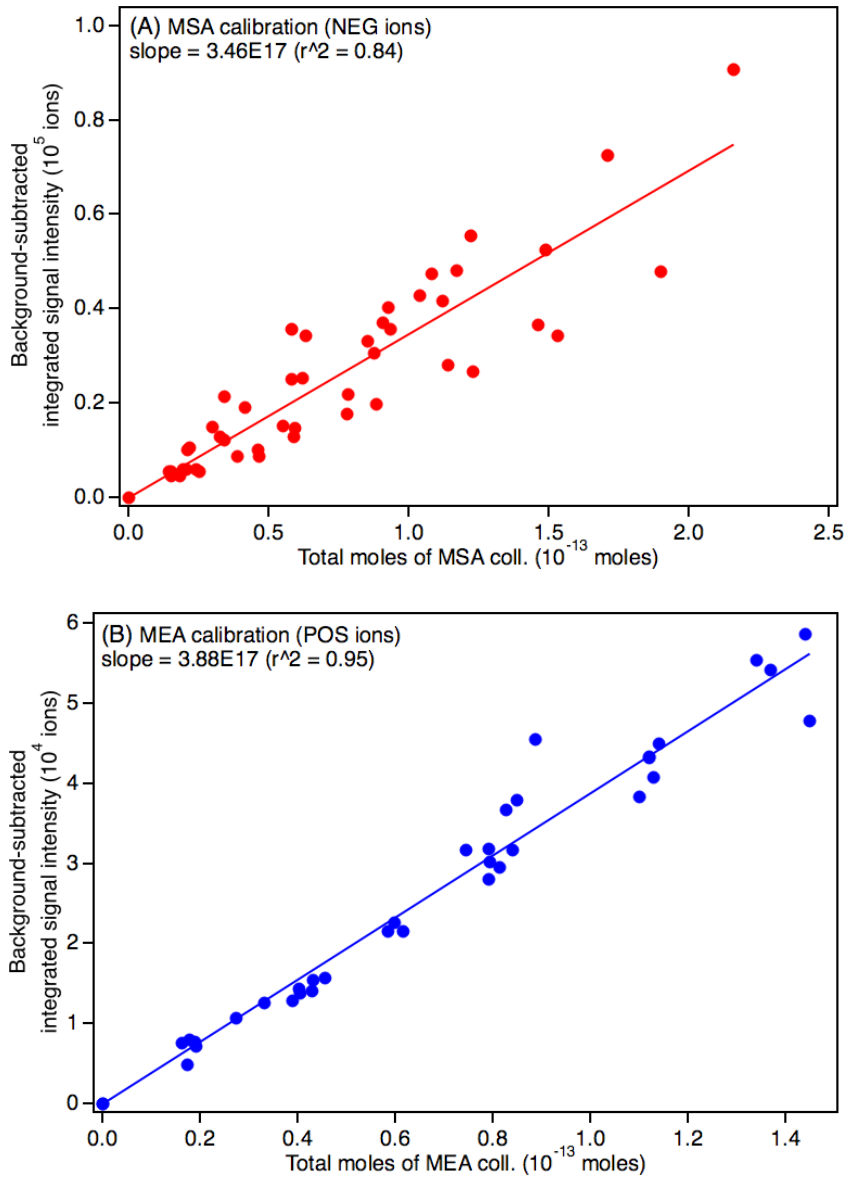

Figure S11. Calibration curves for (A) MEA and (B) MSA obtained from MEA-HCl and MSA-Na atomized particles, respectively, with diameters ranging from 15 to 17 nm.

Summary of the SMPS measurements for the MSA+MEA reaction system

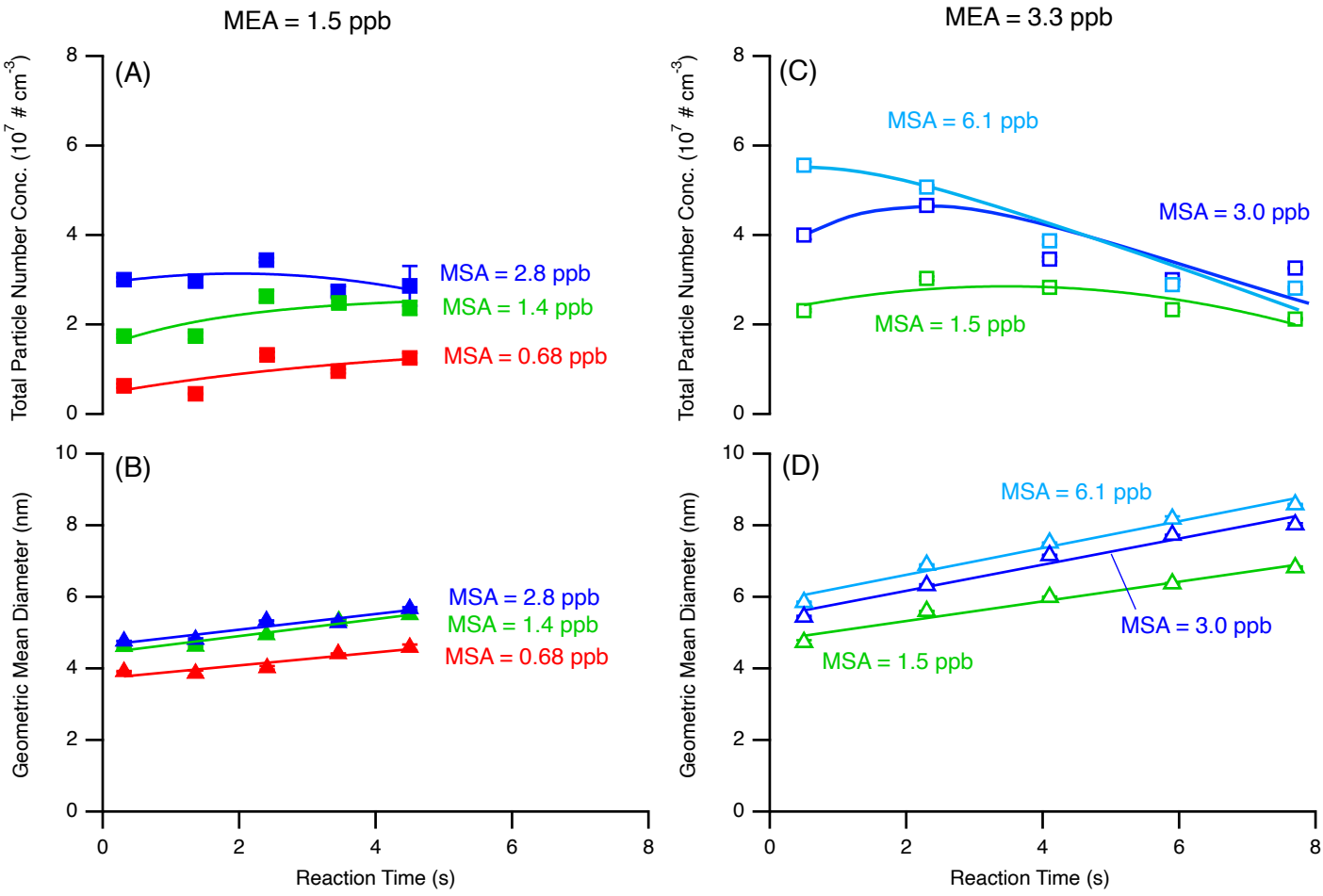

Figure S12. Evolution of the particle total number concentrations and geometric mean diameters observed for the MSA+MEA reaction as a function of the reaction time in the flow reactor. In panels (A) and (C), the lines are guides to the eye, while in panels (B) and (D), the lines are linear fits to the data. All data represent replicate scans (n = 5) and are displayed with one standard deviation. Corresponding size distributions are given in Fig. 1. All measurements were corrected for the losses in the sampling lines.

Influence of relative humidity on the particles formed from the MSA+MEA reaction

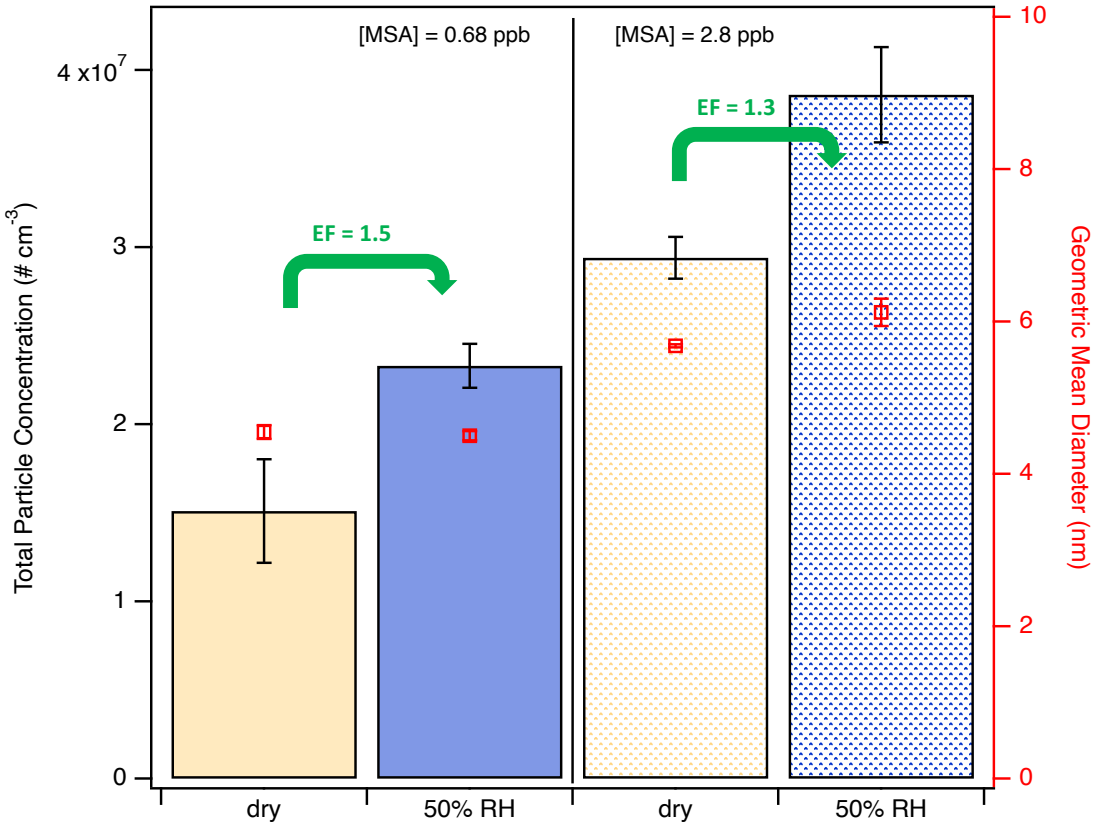

Figure S13. Comparison of the total number concentration (left axis) measured in the MSA+MEA system under either dry conditions (yellow) or in the presence of water vapor corresponding to 50% relative humidity (blue). For all conditions, the MEA concentration is 1.5 ppb. The data for each condition represent the average over 2-5 experiments with the error bar representing one standard variation. Red data points correspond to the averaged geometric mean diameter (right axis) for each condition (± one standard deviation). All measurements were performed at 4.5 s reaction time and were corrected for particle losses through the sampling lines.

Structures, key geometrical parameters (in angstroms), particle charges (in atomic units) and dissociation energies of the most stable MSA-MEA cluster structures

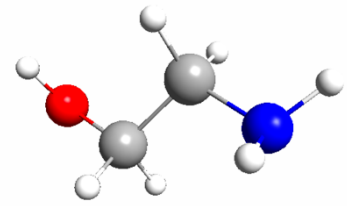

MEA (structure 1)

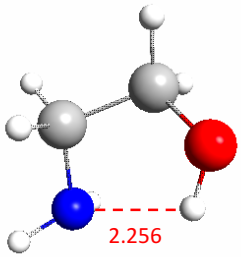

MEA (structure 2)

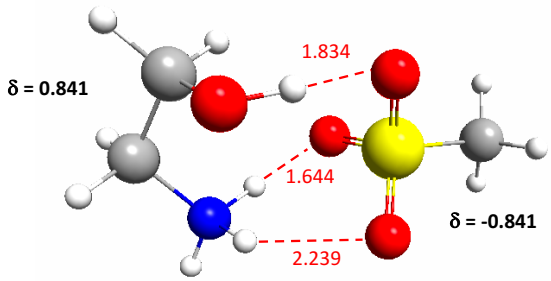

MSA-MEA
ΔE_{diss} = 24.1 kcal/mol

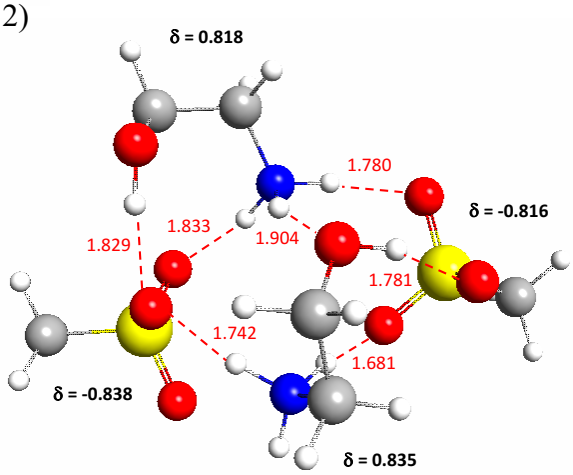

2MSA-2MEA
ΔE_{diss} = 85.5 kcal/mol

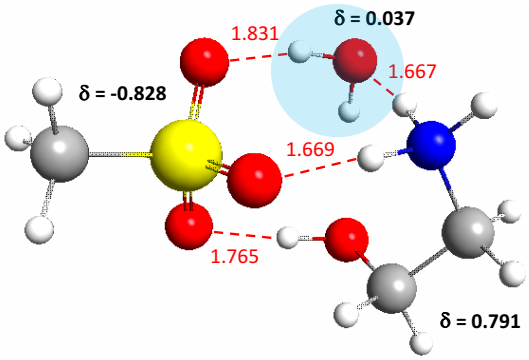

MSA-MEA-H_2O
ΔE_{diss} = 41.6 kcal/mol
$\Delta E_{dehydration}$ = 17.5 kcal/mol

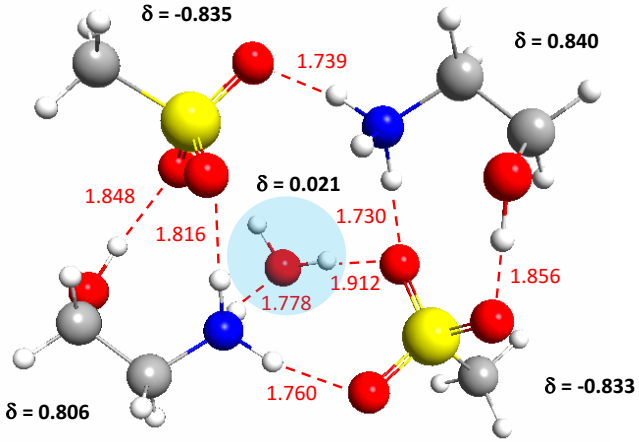

2MSA-2MEA-H_2O
ΔE_{diss} = 99.7 kcal/mol
$\Delta E_{dehydration}$ = 14.2 kcal/mol

Figure S14. Structures, key geometrical parameters including bond length (in angstroms), partial charges (δ; in atomic units) and dissociation energies of the most stable MSA-MEA cluster structures. The initial lowest energy cluster structures were taken from Shen et al.[9] and recalculated using the QChem 4.3 program package[10] using density functional theory (DFT) with the B3LYP hybrid functional[11] and the 6-31+G(d) basis set. Additionally, the DFT-D3(0) dispersion correction from Grimme was used.[12] In this paper, the abbreviation B3LYP-D3/6-31+G(d) is used for this level of theory. Our previous studies showed that this method gives reasonable predictions for geometry and structure, vibrational frequencies, energies, enthalpies, and Gibbs free energies for the MSA-amines clusters.[13-16] Partial charges were calculated at the B3LYP-D3/6-31+G(d) level using natural bond orbital (NBO) analysis.[17,18] All computed energies have been corrected for the zero point energies. Dissociation energies were calculated for the complete dissociation to starting monomers or for the dehydration reaction. Calculations were conducted to illustrate the amount of coordination between molecules inside the MSA-MEA clusters. In all the clusters, the MEA molecule adopts a gauche conformation (structure 2), where the -OH group is facing the $-NH_2$ group, which is lower in energy by 3.28 kcal/mol compared to its other conformer (structure 1), consistent with previous studies.[19] Grey balls correspond to carbon atoms, white is for hydrogen atoms, yellow for sulfur atoms, red for oxygen atoms and blue for nitrogen atoms. Hydrogen bonds are labelled with dashed red lines, and the blue shaded circle highlights the one water molecule in the clusters.

Influence of relative humidity on the particles formed from the MSA+MA reaction

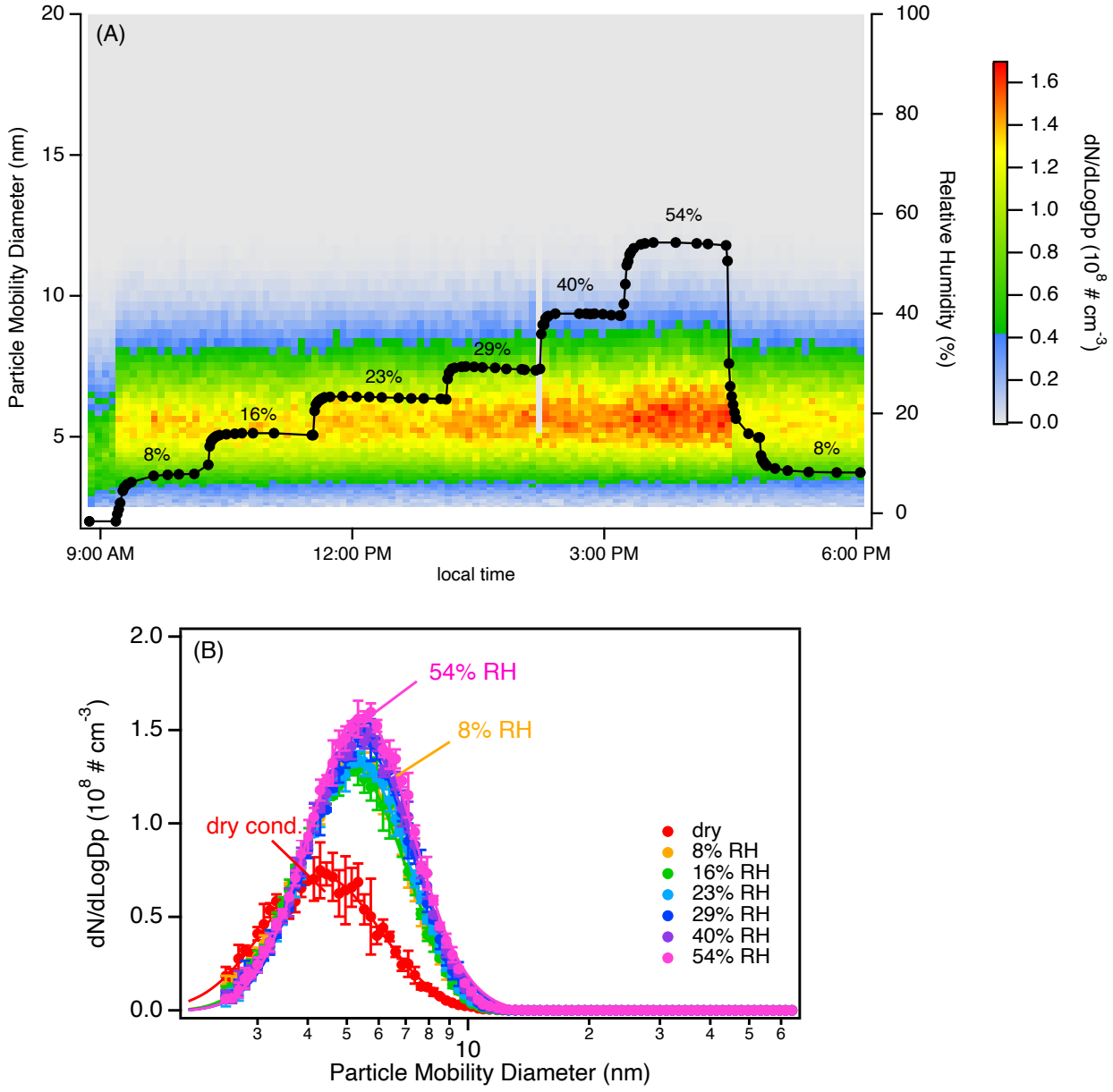

Figure S15. Evolution of the particle size distributions as a function of relative humidity (RH) from the reaction of MSA (1.4 ppb) with MA (10.8 ppb). Panel (A) represents the evolution as a function of time while panel (B) represents snapshots of the size distribution at a given RH (each distribution is an average of 5 replicate SMPS scans with the error bar representing one standard variation). All measurements were performed at 4.5 s reaction time. Particle size distributions were corrected for particle loss through the sampling lines.

References

1. V. Perraud, X. X. Li, J. K. Jiang, B. J. Finlayson-Pitts, J. N. Smith, Size-resolved chemical composition of sub-20 nm particles from methanesulfonic acid reactions with methylamine and ammonia, *ACS Earth Space Chem.,* 2020, **4**, 1182-1194.
2. M. L. Dawson, V. Perraud, A. Gomez, K. D. Arquero, M. J. Ezell, B. J. Finlayson-Pitts, Measurement of gas-phase ammonia and amines in air by collection onto an ion exchange resin and analysis by ion chromatography, *Atmos. Meas. Tech.,* 2014, **7**, 2733-2744.
3. S.-L. von der Weiden, F. Drewnick, S. Borrmann, Particle loss calculator - A new software tool for the assessment of the performace of aerosol inlet systems, *Atmos. Meas. Tech.,* 2009, **2**, 469-494.
4. J. N. Smith, K. F. Moore, P. H. McMurry, F. L. Eisele, Atmospheric measurements of sub-20 nm diameter particle chemical composition by thermal desorption chemical ionization mass spectrometry, *Aerosol Sci. Technol.,* 2004, **38**, 100-110.
5. H. Chen, S. Chee, M. J. Lawler, K. C. Barsanti, B. M. Wong, J. N. Smith, Size resolved chemical composition of nanoparticles from reactions of sulfuric acid with ammonia and dimethylamine, *Aerosol Sci. Technol.,* 2018, **52**, 1120-1133.
6. M. J. Lawler, P. M. Winkler, J. Kim, L. Ahlm, J. Trostl, A. P. Praplan, S. Schobesberger, A. Kuerten, J. Kirkby, F. Bianchi, J. Duplissy, A. Hansel, T. Jokinen, H. Keskinen, K. Lehtipalo, M. Leiminger, T. Petaja, M. Rissanen, L. Rondo, M. Simon, M. Sipila, C. Williamson, D. Wimmer, I. Riipinen, A. Virtanen, J. N. Smith, Unexpectedly acidic nanoparticles formed in dimethylamine-ammonia-sulfuric-acid nucleation experiments at CLOUD, *Atmos. Chem. Phys.,* 2016, **16**, 13601-13618.
7. J. K. Jiang, C. M. Kim, X. L. Wang, M. R. Stolzenburg, S. L. Kaufman, C. L. Qi, G. J. Sem, H. Sakurai, N. Hama, P. H. McMurry, Aerosol charge fractions downstream of six bipolar chargers: effects of ion source, source activity, and flowrate, *Aerosol Sci. Technol.,* 2014, **48**, 1207-1216.
8. V. Perraud, J. Olfert, J. N. Smith, Effective density measurement of sodium methanesulfonate and aminium chloride nanoparticles, *Aerosol Sci. Technol.,* 2022, **57**, 355-366.
9. J. Shen, H.-B. Xie, J. Elm, F. Ma, J. Chen, H. Vehkamaki, Methanesulfonic acid-driven new particle formation enhanced by monoethanolamine: A computational study, *Environ. Sci. Technol.,* 2019, **53**, 14387-14397.
10. Y. H. Shao, Z. T. Gan, E. Epifanovsky, A. T. B. Gilbert, M. Wormit, J. Kussmann, A. W. Lange, A. Behn, J. Deng, X. T. Feng, D. Ghosh, M. Goldey, P. R. Horn, L. D. Jacobson, I. Kaliman, R. Z. Khaliullin, T. Kus, A. Landau, J. Liu, E. I. Proynov, Y. M. Rhee, R. M. Richard, M. A. Rohrdanz, R. P. Steele, E. J. Sundstrom, H. L. Woodcock, P. M. Zimmerman, D. Zuev, B. Albrecht, E. Alguire, B. Austin, G. J. O. Beran, Y. A. Bernard, E. Berquist, K. Brandhorst, K. B. Bravaya, S. T. Brown, D. Casanova, C. M. Chang, Y. Q. Chen, S. H. Chien, K. D. Closser, D. L. Crittenden, M. Diedenhofen, R. A. DiStasio, H. Do, A. D. Dutoi, R. G. Edgar, S. Fatehi, L. Fusti-Molnar, A. Ghysels, A. Golubeva-Zadorozhnaya, J. Gomes, M. W. D. Hanson-Heine, P. H. P. Harbach, A. W. Hauser, E. G. Hohenstein, Z. C. Holden, T. C. Jagau, H. J. Ji, B. Kaduk, K. Khistyaev, J. Kim, J.

Kim, R. A. King, P. Klunzinger, D. Kosenkov, T. Kowalczyk, C. M. Krauter, K. U. Lao, A. D. Laurent, K. V. Lawler, S. V. Levchenko, C. Y. Lin, F. Liu, E. Livshits, R. C. Lochan, A. Luenser, P. Manohar, S. F. Manzer, S. P. Mao, N. Mardirossian, A. V. Marenich, S. A. Maurer, N. J. Mayhall, E. Neuscamman, C. M. Oana, R. Olivares-Amaya, D. P. O'Neill, J. A. Parkhill, T. M. Perrine, R. Peverati, A. Prociuk, D. R. Rehn, E. Rosta, N. J. Russ, S. M. Sharada, S. Sharma, D. W. Small, A. Sodt, T. Stein, D. Stück, Y. C. Su, A. J. W. Thom, T. Tsuchimochi, V. Vanovschi, L. Vogt, O. Vydrov, T. Wang, M. A. Watson, J. Wenzel, A. White, C. F. Williams, J. Yang, S. Yeganeh, S. R. Yost, Z. Q. You, I. Y. Zhang, X. Zhang, Y. Zhao, B. R. Brooks, G. K. L. Chan, D. M. Chipman, C. J. Cramer, W. A. Goddard, M. S. Gordon, W. J. Hehre, A. Klamt, H. F. Schaefer, M. W. Schmidt, C. D. Sherrill, D. G. Truhlar, A. Warshel, X. Xu, A. Aspuru-Guzik, R. Baer, A. T. Bell, N. A. Besley, J. D. Chai, A. Dreuw, B. D. Dunietz, T. R. Furlani, S. R. Gwaltney, C. P. Hsu, Y. S. Jung, J. Kong, D. S. Lambrecht, W. Z. Liang, C. Ochsenfeld, V. A. Rassolov, L. V. Slipchenko, J. E. Subotnik, T. Van Voorhis, J. M. Herbert, A. I. Krylov, P. M. W. Gill, M. Head-Gordon, Advances in molecular quantum chemistry contained in the Q-Chem 4 program package, *Mol. Phys.,* 2015, **113**, 184-215.

11. A. D. Becke, Density-Functional Thermochemistry .3. The Role of Exact Exchange, *J. Chem. Phys.,* 1993, **98**, 5648-5652.
12. S. Grimme, J. Antony, S. Ehrlich, H. Kried, A consistent and accurate ab initio parametrization of density functional dispersion correction (DFT-D) for the 94 elements H-Pu, *J. Chem. Phys.,* 2010, **132**, Art No 154104 (154101-154119).
13. J. Xu, V. Perraud, B. J. Finlayson-Pitts, R. B. Gerber, Uptake of water by an acid-base nanoparticle: theoretical and experimental studies of the methanesulfonic acid-methylamine system, *Phys. Chem. Chem. Phys.,* 2018, **20**, 22249-22259.
14. J. Xu, B. J. Finlayson-Pitts, R. B. Gerber, Proton transfer in mixed clusters of methanesulfonic acid, methylamine, and oxalic acid: implications for atmospheric particle formation, *J. Phys. Chem. A,* 2017, **121**, 2377-2385.
15. H. Chen, M. E. Varner, R. B. Gerber, B. J. Finlayson-Pitts, Reactions of methanesulfonic acid with amines and ammonia as a source of new particles in air, *J. Phys. Chem. B,* 2016, **120**, 1526-1536.
16. M. L. Dawson, M. E. Varner, V. Perraud, M. J. Ezell, R. B. Gerber, B. J. Finlayson-Pitts, Simplified mechanism for new particle formation from methanesulfonic acid, amines, and water via experiments and ab initio calculations, *Proc. Natl. Acad. Sci. USA,* 2012, **109**, 18719-18724.
17. J. P. Foster, F. Weinhold, Natural hybrid orbitals, *J. Am. Chem. Soc.,* 1980, **102**, 7211-7218.
18. A. E. Reed, F. Weinhold, Natural bond orbital analysis of nearHartree-Fock water dimer, *J. Chem. Phys.,* 1983, **78**, 4066-4073.
19. C. F. P. Silva, M. L. T. S. Duarte, R. Fausto, A concerted SCF-MO ab initio and vibrational spectroscopic study of the conformational isomerism in 2-aminoethanol, *J. Mol. Struct.,* 1999, **482**, 591-599.